# van der Waals contact between nucleophile and transferring phosphorus is insufficient to achieve enzyme transition state architecture

*Luke A. Johnson,*[†,¥,#] *Angus J. Robertson,*[†,#] *Nicola J. Baxter,*[†,‡] *Clare R. Trevitt,*[†] *Claudine Bisson,*[†,§] *Yi Jin,*[†,¥] *Henry P. Wood,*[†] *Andrea M. Hounslow,*[†] *Matthew J. Cliff,*[‡] *G. Michael Blackburn,*[†] *Matthew W. Bowler,*[‖] *and Jonathan P. Waltho,*[†,‡,*]

[†] Krebs Institute for Biomolecular Research, Department of Molecular Biology and Biotechnology, The University of Sheffield, Sheffield, S10 2TN, United Kingdom

[‡] Manchester Institute of Biotechnology and School of Chemistry, The University of Manchester, Manchester, M1 7DN, United Kingdom

[‖] European Molecular Biology Laboratory, Grenoble Outstation, 71 avenue des Martyrs, CS 90181 F-38042 Grenoble, France

## ABSTRACT

Phosphate plays a crucial role in biology, owing to the stability of the phosphate ester bond. To overcome this inherent stability, enzymes that catalyze phosphoryl transfer reactions achieve enormous rate accelerations to operate on biologically relevant timescales and the mechanisms that underpin catalysis have been the subject of extensive debate. In an archetypal system, β-phosphoglucomutase catalyzes the reversible isomerization of β-glucose 1-phosphate and glucose 6-phosphate *via* two phosphoryl transfer steps using a β-glucose 1,6-bisphosphate intermediate and a catalytic $Mg^{II}$ ion. In the present work, a variant of β-phosphoglucomutase, where the aspartate residue that acts as a general acid-base is replaced with asparagine, traps highly stable complexes containing the β-glucose 1,6-bisphosphate intermediate in the active site. Crystal structures of these complexes show that, when the enzyme is unable to transfer a proton, the intermediate is arrested in catalysis at an initial stage of phosphoryl transfer. The nucleophilic oxygen and transferring phosphorus atoms are aligned and in van der Waals contact, yet the enzyme is less closed than in transition state (analogue) complexes and binding of the catalytic $Mg^{II}$ ion is compromised. Together, these observations indicate that optimal closure and optimal $Mg^{II}$ binding occur only at higher energy positions on the reaction trajectory, allowing the enzyme to balance efficient catalysis with product dissociation. It is also confirmed that the general acid-base ensures that mutase activity is ~$10^3$ fold greater than phosphatase activity in β-phosphoglucomutase.



## KEYWORDS

phosphoryl transfer enzyme | general acid-base catalysis | near attack conformation | magnesium ion affinity | X-ray crystallography

## INTRODUCTION

The efficiency of phosphoryl transfer enzymes in overcoming the stability of phosphate mono- and di-esters under physiological conditions has enabled biology to perform a vast array of functions, spanning transient cell signaling cascades, energy storage and consumption, protein regulation and the manipulation of genetic material (*1*). Phosphoryl transfer enzymes can achieve catalytic rate constants ($k_{cat}$) of greater than 100 $s^{-1}$, even when spontaneous rate constants are as low as $10^{-20}$ $s^{-1}$. As such, they possess some of the largest enzymatic accelerations identified, with catalytic enhancements approaching $10^{21}$ (*2*). Part of these accelerations has often been ascribed to general acid-base catalysis that both augments phosphorylation rates by assisting deprotonation of the nucleophilic hydroxyl oxygen, and enhances dephosphorylation rates by aiding protonation of the same oxygen atom (now the bridging oxygen of the phosphate group). Residues that satisfy the assignment of the general acid-base (commonly aspartate, glutamate or histidine residues) are repeatedly conserved in the active sites of multiple superfamilies of phosphoryl transfer enzymes and are consistently identified by mutation studies as key elements of enzyme activity (*3*−*8*). While structural studies reveal the close proximity of the general acid-base to reacting groups in near-transition state complexes, the precise relationship of proton transfer to the mechanism of the phosphoryl transfer reaction remains uncertain. Density-functional theory (DFT) models of the phosphoryl transfer step in some enzymes predict that proton transfer occurs only when there is substantial bond formation between the hydroxyl nucleophile and the phosphorus atom (*9*−*13*), but conclusions based on DFT models depend on how closely the protein conformation reflects that in which proton transfer takes place. However, solvent deuterium isotope effect measurements and the pH dependence of pre-steady state kinetic analyses often support the DFT models in that the rate of phosphoryl transfer is interpreted to be

independent of hydroxyl nucleophile deprotonation (*14*−*16*). A resolution of the uncertainty over how the proton transfer step contributes to the catalytic cycle requires direct structural evidence of the protein conformation in which proton transfer occurs.

β-phosphoglucomutase (βPGM) from *Lactococcus lactis* is a well-studied magnesium-dependent phosphoryl transfer enzyme of the haloacid dehalogenase (HAD) superfamily (*8, 17*−*23*), which catalyzes the reversible isomerization of β-glucose 1-phosphate (βG1P) and glucose 6-phosphate (G6P) (Figure 1A). The active site is located in the cleft formed between the helical cap domain (T16−V87) and the α/β core domain (M1−D15, S88−K216), with closure of the cleft through domain reorientation occurring during catalysis. The active site binds two phosphate groups, one in the *proximal* site adjacent to D8 and the catalytic $Mg^{II}$ ion, and one in the *distal* site (~8 Å away in the closed enzyme). βPGM transfers a phosphate group from the phospho-enzyme ($\beta PGM^{P}$, phosphorylated on the carboxylate sidechain of residue D8) to the physiological substrate, βG1P, (Step 1; (*19*)) forming an enzyme-bound β-glucose 1,6-bisphosphate (βG16BP) intermediate (*18*). Subsequent release of βG16BP to solution permits its binding in the alternate orientation, leading to dephosphorylation of βG16BP (Step 2; (*20*)) and the generation of G6P and $\beta PGM^{P}$ as products (Figure 1A). In the Step 1 complexes, βPGM hydrogen bonds to the substrate directly, whereas in the Step 2 complexes, two water molecules mediate hydrogen bonding with substrate (*19*). Structural investigations of species along the reaction coordinate have made extensive use of metal fluoride-based ground and transition state analogue complexes (*24*, *25*), and have experimentally corroborated the in-line nucleophilic attack of phosphoryl transfer, the trigonal bipyramidal nature of the chemical transition state (TS), and the requirement for charge balance in the active site (*20*−*22*). Moreover, these studies

have highlighted how the carboxylate group of the assigned general acid-base (residue D10) can adopt different orientations (*8*). In substrate-free βPGM and $\beta PGM^P$ analogue structures (*20, 23*), the active site cleft is open and the D10 carboxylate is in the *out* position (Figure 1B). In transition state analogue (TSA) structures (*20*), domain reorientation has closed the active site cleft and the D10 carboxylate is in the *in* position, where it is positioned to facilitate general acid-base catalysis. In the substrate-bound $\beta PGM^P$ analogue structures containing $BeF_3^-$ (*23*) two conformations are observed, in both of which the active site cleft is closed. One has the same conformation as the TSA structures, while in the other the cap and core domains have a relative rotation of 17° and the D10 carboxylate is in the *out* position. Both of the substrate-bound $\beta PGM^P$ analogue structures conform to the criteria of near attack conformations (NACs) (*26*). The TSA-like conformation is termed an aligned NAC as the nucleophile is aligned to attack the $BeF_3^-$ moiety, whereas the rotated conformation is termed a hydrogen-bonded NAC as the nucleophilic hydroxyl group is hydrogen bonded to the $BeF_3^-$ moiety (*23*). The observation of both NACs supports a model where the conformational change between the two closed forms is correlated with the *out* to *in* transition of D10 and the alignment of the substrate for nucleophilic attack.

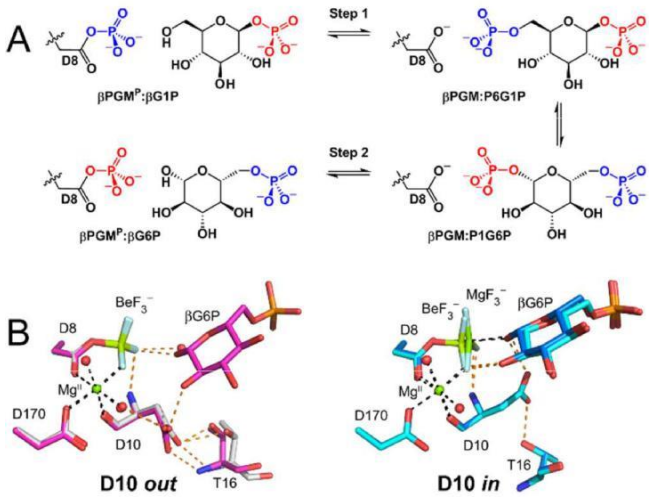


**Figure 1.** The βPGM reaction scheme and change in orientation of residue D10, the assigned general acid-base. (A) βPGM reaction scheme for the enzymatic conversion of βG1P to G6P *via* a βG16BP intermediate. The phosphoryl transfer reaction between the phospho-enzyme ($\beta PGM^P$, phosphorylated at residue D8) and βG1P is termed Step 1 and is illustrated with the transferring phosphate (blue) in the *proximal* site and the 1-phosphate (red) of βG1P in the *distal* site. The equivalent reaction between $\beta PGM^P$ and G6P is termed Step 2 and is shown with the transferring phosphate (red) in the *proximal* site and the 6-phosphate (blue) of G6P in the *distal* site. The two intermediate complexes are labeled βPGM:P6G1P and βPGM:P1G6P to explicitly denote the orientation of βG16BP bound in the active site. (B) The carboxylate group of residue D10 is in the *out* position in both the open substrate-free $\beta PGM^P$ analogue structure (βPGM:$BeF_3$ complex; PDB 2WFA (*23*); gray carbon atoms) and in the hydrogen bonded NAC (βPGM:$BeF_3$:G6P complex; PDB 2WF9 (*23*); magenta carbon atoms). In contrast, the carboxylate group of residue D10 is in the *in* position in both the transition state analogue (TSA) structure (βPGM:$MgF_3$:G6P TSA complex; PDB 2WF5 (*20*); blue carbon atoms) and in the aligned NAC (βPGM:$BeF_3$:G6P complex; PDB 2WF8 (*23*); cyan carbon atoms). Selected active

site residues and ligand are shown as sticks in standard CPK colors, with beryllium (light green), magnesium (green) and fluorine (light blue). Structural waters (red) and the catalytic $Mg^{II}$ ion (green) are drawn as spheres. Orange dashes indicate hydrogen bonds and black dashes show metal ion coordination.

The models above require extrapolation from the behavior of metal fluoride analogues in the active site to that of the substrates. While there is growing computational evidence for a close relationship between metal fluoride TSA complexes and the corresponding phosphoryl species (*27*, *28*), there are few experimental systems where the properties of both species can be examined in detail. In order to address this, we sought to establish a stable enzyme:substrate complex using an aspartate to asparagine substitution, in a system for which the behavior of metal fluoride analogue complexes is well determined (*20*, *23*). Here, we report the properties of several complexes involving the βPGM D10N variant ($\beta PGM_{D10N}$), which serves as a model of wild-type βPGM ($\beta PGM_{WT}$) with the general acid-base in its protonated form. This variant has previously been reported to be inactive (*8*), and was expected to offer the opportunity to study $\beta PGM^{P}$:βG1P, $\beta PGM^{P}$:G6P and βPGM:βG16BP complexes independently. Here we show that the $\beta PGM_{D10N}$ variant purifies as $\beta PGM_{D10N}$:βG16BP complexes. Low-level mutase activity was observed, which was enhanced once the non-covalently-bound intermediate is removed by denaturation-refolding. Subsequently, exposure to substrate leads to the reformation of $\beta PGM_{D10N}$:βG16BP complexes in solution, and the trapping of two distinct $\beta PGM_{D10N}$:βG16BP complexes *in crystallo*, with either the 1- or the 6-phosphate group in the *proximal* site. In both of these complexes, the nucleophilic carboxylate oxygen and the phosphorus atoms are aligned and in van der Waals contact, but phosphoryl transfer is arrested by the failure of N10 to release

a proton to βG16BP. However, the $\beta PGM_{D10N}$:βG16BP complexes do not adopt the fully closed conformation of the TSA complexes, indicating that such close proximity between reacting groups is insufficient to achieve the architecture used by the enzyme to bind the TS. Remarkably, the binding affinity of the catalytic $Mg^{II}$ ion in the $\beta PGM_{D10N}$:βG16BP complexes is reduced compared to the phospho-enzyme analogue and the TSA complexes, which implies that antagonism within the coordination of the $Mg^{II}$ ion facilitates the release of the high affinity βG16BP intermediate.

## EXPERIMENTAL METHODS

**β-Phosphoglucomutase (βPGM) expression, purification and refolding.** Site-directed mutagenesis (QuikChange II kit, Agilent Technologies) of the βPGM gene from *Lactococcus lactis* (EC 5.4.2.6) cloned in a pET22b+ vector was employed to generate the D10N variant ($\beta PGM_{D10N}$) and the D8N variant ($\beta PGM_{D8N}$) using primers with single-site base changes and mutagenesis of the βPGM gene was confirmed by DNA sequencing. Wild-type βPGM ($\beta PGM_{WT}$), $\beta PGM_{D10N}$ and $\beta PGM_{D8N}$ proteins were expressed using natural abundance, $^{15}N$ or $^{2}H^{15}N^{13}C$ isotopic enrichment (*21*, *29*) and purified using the following methodology which minimized the presence of contaminating phosphoryl transfer enzymes (*e.g.*, phosphoglucose isomerase and βPGM from *E. coli*). The cell pellet was resuspended in ice-cold standard native buffer (50 mM $K^+$ HEPES (pH 7.2), 5 mM $MgCl_2$, 2 mM $NaN_3$) supplemented with one tablet of cOmplete™ protease inhibitor cocktail (Roche). The cell suspension was lysed on ice by sonication for 5 cycles of pulsation for 20 s with 60 s cooling intervals. The cell lysate was then separated by ultracentrifugation (Beckman Coulter Avanti centrifuge) at 24,000 rpm for 35 min

at 4 °C. The cleared cell lysate was filtered using a 0.2 μM syringe filter and loaded onto a DEAE-Sepharose fast flow ion-exchange column connected to an ÄKTA purification system that had been washed previously with 1 column volume of 6 M guanidine hydrochloride, 1 column volume of 1 M NaOH and equilibrated with 5 column volumes of standard native buffer. Following extensive washing, proteins bound to the DEAE-Sepharose column were eluted with a gradient of 0 to 100% standard native buffer containing 0.5 M NaCl. Fractions containing βPGM were checked for purity using SDS-PAGE, were pooled together and concentrated by Vivaspin (10 kDa MWCO). The protein sample was filtered using a 0.2 μM syringe filter and loaded onto a prepacked Hiload 26/60 Superdex 75 size-exclusion column connected to an ÄKTA purification system that had been washed previously with 1 column volume of 1 M NaOH and equilibrated with 5 column volumes of filtered and degassed standard native buffer containing 1 M NaCl. Fractions containing βPGM were checked for purity using SDS-PAGE, were pooled together, buffer exchanged into standard native buffer and concentrated to 2 mM by Vivaspin (10 kDa MWCO) for storage as 1 mL aliquots at −20 °C.

In contrast to $\beta PGM_{WT}$ and $\beta PGM_{D8N}$, $\beta PGM_{D10N}$ co-purified with βG16BP as tight, non-covalently bound $\beta PGM_{D10N}$:βG16BP complexes. Substrate-free $\beta PGM_{D10N}$ was prepared from the co-purified $\beta PGM_{D10N}$:βG16BP complexes using an unfolding-dilution-refolding strategy to remove βG16BP. Samples of the co-purified $\beta PGM_{D10N}$:βG16BP complexes were diluted into unfolding buffer (4 M guanidine hydrochloride, 50 mM $K^+$ HEPES (pH 7.2), 5 mM $MgCl_2$, 2 mM $NaN_3$), buffer exchanged by Vivaspin (10 kDa MWCO) in unfolding buffer to dilute βG16BP by 200-fold, and the retained $\beta PGM_{D10N}$ was refolded by pulse renaturation or dialysis into standard native buffer. A final buffer exchange to remove any remaining denaturant was

performed using a Vivaspin (3 kDa MWCO) and the protein was concentrated to 2 mM for storage as 1 mL aliquots at −20 °C. Removal of βG16BP from $\beta PGM_{D10N}$ was confirmed by $^{31}P$ NMR spectroscopy in standard NMR buffer (50 mM $K^+$ HEPES (pH 7.2), 5 mM $MgCl_2$, 2 mM $NaN_3$, 10% (v/v) $^2H_2O$ and 1 mM trimethylsilyl propanoic acid (TSP)).

The reconstituted $\beta PGM_{D10N}$:βG16BP complexes were formed by the addition of 20 mM acetyl phosphate (AcP) and 10 mM glucose 6-phosphate (G6P) or 10 mM β-glucose 1-phosphate (βG1P) to 1 mM substrate-free $\beta PGM_{D10N}$ in 200 mM $K^+$ HEPES buffer (pH 7.2), 5 mM $MgCl_2$ and 2 mM $NaN_3$. Unbound ligands in the sample (excess G6P, βG1P and AcP) were removed by buffer exchange into standard NMR buffer.

**Reagents.** Unless otherwise stated, reagents were purchased from Sigma-Aldrich, GE Healthcare, Melford Laboratories or CortecNet.

βG16BP was isolated from the co-purified $\beta PGM_{D10N}$:βG16BP complexes in standard NMR buffer by heat denaturation of $\beta PGM_{D10N}$ (2 min at 80 °C), centrifugation at 13,000 rpm to remove denatured $\beta PGM_{D10N}$ and filtration of the supernatant containing βG16BP using a Vivaspin (3 kDa MWCO). Resonance assignments of βG16BP were confirmed by $^{31}P$ and natural abundance $^1H^{13}C$ HSQC NMR spectra following the addition of 6 mM EDTA to the sample.

βG1P was synthesized enzymatically from maltose using maltose phosphorylase (EC 2.4.1.8). 1 M maltose was incubated overnight at 30 °C with 1.5 units $mL^{-1}$ maltose phosphorylase in 0.5 M phosphate buffer (pH 7.0). βG1P production was confirmed using $^{31}P$ NMR spectroscopy. Maltose phosphorylase (90 kDa) was removed using a Vivaspin (5 kDa MWCO) and the resulting flow-through solution containing βG1P was used without further purification. The concentration of βG1P was measured to be 150 mM by quantitative $^{31}P$ NMR spectroscopy

(recycle time 60 s) against a known concentration of G6P. The concentrations of other components in the solution were estimated as follows: 150 mM glucose, 850 mM maltose and 350 mM inorganic phosphate.

Uniformly $^{13}$C-labeled G6P was synthesized enzymatically from 45 mM uniformly $^{13}$C-labeled D-glucose by incubation for 90 min at 37 °C with 14 units $mL^{-1}$ hexokinase (EC 2.7.1.1) and 50 mM ATP in 100 mM Tris-HCl (pH 8.0), 50 mM $MgCl_2$ and 2 mM EDTA. G6P production was confirmed using $^{31}$P NMR spectroscopy. Hexokinase (110 kDa) was removed by denaturation at 80 °C followed by filtration using a Vivaspin (3 kDa MWCO). The flow-through containing uniformly $^{13}$C-labeled G6P was used without further purification together with AcP and substrate-free$\beta PGM_{D10N}$ for the formation of uniformly $^{13}$C-labeled βG16BP in the reconstituted $\beta PGM_{D10N}$:βG16BP complexes.

Chemically synthesized βG16BP was a gift from Prof. Nicholas Williams, Department of Chemistry, The University of Sheffield (*30*).

**NMR spectroscopy.**

**Instruments and data processing.** NMR experiments were acquired at 298 K using Bruker spectrometers located at the following institutions: Department of Molecular Biology and Biotechnology (MBB), The University of Sheffield; School of Chemistry (SC), The University of Manchester; Manchester Institute of Biotechnology (MIB), The University of Manchester. Experiments were processed using TopSpin (Bruker) or FELIX (Felix NMR, Inc.) and figures were prepared using either FELIX or CcpNmr Analysis (*31*). $^{1}$H chemical shifts were referenced relative to the internal TSP signal resonating at 0.0 ppm and $^{13}$C, $^{15}$N and $^{31}$P chemical shifts were referenced indirectly using nuclei-specific gyromagnetic ratios.

**$^{1}H^{15}N$ TROSY spectra.** $^{1}H^{15}N$ TROSY spectra of $\beta PGM_{WT}$ and substrate-free $\beta PGM_{D10N}$ were acquired using 0.5 – 1 mM $^{15}N$-βPGM in standard NMR buffer (50 mM $K^+$ HEPES (pH 7.2), 5 mM $MgCl_2$, 2 mM $NaN_3$ with 10% (v/v) $^{2}H_2O$ and 2 mM TSP) containing 50 mM $MgCl_2$. $^{1}H^{15}N$ TROSY spectra of the $\beta PGM_{WT}$:$BeF_3$ and $\beta PGM_{D10N}$:$BeF_3$ complexes were acquired using 0.5 – 1 mM $^{15}N$-$\beta PGM_{WT}$ or $^{15}N$-substrate-free $\beta PGM_{D10N}$ in standard NMR buffer containing 5 mM $BeCl_2$ and 10 mM $NH_4F$. Experiments were recorded using a Bruker 600 MHz Avance DRX spectrometer equipped with a TXI cryoprobe and z-axis gradients (MBB) or a Bruker 800 MHz Avance I spectrometer equipped with a TXI probe and z-axis gradients (MBB).

**$^{31}P$ spectra.** One-dimensional $^{31}P$ spectra to characterize βG16BP and the $\beta PGM_{D10N}$:βG16BP complexes were acquired using a Bruker 500 MHz Avance DRX spectrometer (operating at 202.456 MHz for $^{31}P$) equipped with a broadband probe (MBB). A spectral width of 50 ppm centered at −10 ppm enabled the observation of the relevant phosphorus signals. Typically, accumulations of 10,000 transients without proton-phosphorus decoupling were necessary to achieve a sufficient signal-to-noise ratio with sample concentrations in the 0.5 – 1 mM range. Spectra were processed with baseline correction and 10 Hz Lorentzian apodization.

**$^{31}P$ spectra for kinetic measurements.** Reaction kinetics for βPGM-catalyzed reactions were followed using a Bruker 500 MHz Avance III HD spectrometer (operating at 202.48 MHz for $^{31}P$) equipped with a Prodigy BBO cryoprobe (SC), which offered significant improvements in signal sensitivity. One-dimensional $^{31}P$ spectra without proton-phosphorus decoupling were recorded within 1 minute, with 16 transients and a 2 s recycle delay to give signal-to-noise ratios for 10 mM βG1P of greater than 100:1. The equilibrations of 10 mM βG1P with G6P by 0.1 – 1 μM $\beta PGM_{WT}$, 5 − 50 μM substrate-free $\beta PGM_{D10N}$ and 10 μM $\beta PGM_{D8N}$ were measured in standard kinetic buffer (200 mM $K^+$ HEPES buffer (pH 7.2), 5 mM $MgCl_2$, 2 mM $NaN_3$, 10%

$^{2}H_2O$ and 2 mM TSP). The reaction was initiated by and timed from the addition of 20 mM AcP and monitored by the acquisition of consecutive $^{31}P$ spectra. The equilibration of 10 mM βG1P with G6P by 5 μM substrate-free $βPGM_{D10N}$ using βG16BP extracted from the co-purified $βPGM_{D10N}$:βG16BP complexes as a priming agent was measured in standard kinetic buffer monitored by one-dimensional $^{31}P$ spectra recorded without proton-phosphorus decoupling with 256 transients and a 1 s recycle delay using a Bruker 500 MHz Avance DRX spectrometer (MBB). Normalized integral values of both the βG1P and G6P peaks following baseline correction and 2 Hz Lorentzian apodization were plotted against time to give kinetic profiles. The linear steady-state portion of the G6P integral data was fitted using a linear least-squares fitting algorithm to derive the catalytic rate constant, $k_{cat}$. The hydrolysis kinetics of 50 mM AcP to inorganic phosphate and acetate by 250 μM βPGM was measured in standard kinetic buffer containing 50 mM $MgCl_2$ and 1 mM EDTA. The reaction was timed from the addition of AcP and monitored by the acquisition of consecutive $^{31}P$ spectra. Normalized integral values of the AcP peak following baseline correction and 2 Hz Lorentzian apodization were plotted against time and the rate constant for AcP hydrolysis was derived from linear least-squares fitting of the data. A control experiment involving 50 mM AcP alone in standard kinetic buffer established that hydrolysis of AcP was insignificant over the same timeframe. Throughout all the kinetic measurements, the pH of the reactions was found to be invariant as assessed *in situ* by the $^{31}P$ resonance of inorganic phosphate and the $^{1}H$ resonances of 200 mM HEPES buffer.

**$^{1}H^{13}C$ HSQC and 2D CCH-TOCSY spectra of glucose 1,6-bisphosphate species.** Natural abundance $^{1}H^{13}C$ HSQC spectra of αG16BP and βG16BP (in 100% $^{2}H_2O$ and 1 mM TSP) were recorded on a Bruker 500 MHz Avance DRX spectrometer equipped with a TXI probe and z-axis gradients (MBB) (*30*). To assign the bound βG16BP resonances in the reconstituted

βPGM$_{D10N}$:βG16BP complexes, $^{1}H^{13}C$ HSQC and 2D CCH-TOCSY spectra were acquired with 0.5 – 1 mM $^{15}N$-labeled substrate-free βPGM$_{D10N}$ in standard NMR buffer containing 20 mM AcP and 10 mM uniformly $^{13}C$-labeled G6P using a Bruker Avance III 800 MHz spectrometer equipped with a TCI cryoprobe and z-axis gradients (MIB).

**$^{1}H^{15}N$ BEST-TROSY experiments.** Rapid acquisition $^{1}H^{15}N$ BEST-TROSY spectra (*32*, *33*) to follow βPGM$_{D10N}$-catalyzed reactions were acquired using 1 mM substrate-free βPGM$_{D10N}$ in standard kinetic buffer containing either 20 mM AcP or 20 mM AcP and 10 mM βG1P. $^{1}H^{15}N$ BEST-TROSY spectra were recorded using a Bruker 600 MHz Avance DRX spectrometer equipped with a TXI cryoprobe and z-axis gradients (MBB) as 6 minute experiments (4 transients, 200 increments and a recycle delay of 0.3 s) with selective $^{1}H$ pulses centered on the amide region (8.7 ppm). Excitation pulses (90°) were 2 ms at 600 MHz (pulse shape Pc9_4) and 1.7 ms at 600 MHz (pulse shape Eburp2), whereas refocusing pulses (180°) were 1.6 ms at 600 MHz (pulse shape Reburp). The experimental dead-time was approximately 6 minutes.

**Backbone resonance assignment of the βPGM$_{D10N}$:βG16BP complexes.** For the $^{1}H$, $^{13}C$ and $^{15}N$ backbone resonance assignment of the reconstituted βPGM$_{D10N}$:βG16BP complexes, multi-dimensional heteronuclear NMR spectra were acquired with 0.5 – 1 mM $^{2}H^{15}N^{13}C$-labeled substrate-free βPGM$_{D10N}$ in standard NMR buffer containing 20 mM AcP and 10 mM G6P using a Bruker 800 MHz Avance III spectrometer equipped with a TCI cryoprobe and z-axis gradients (MIB). The standard suite of $^{1}H^{15}N$-TROSY and 3D TROSY-based constant time experiments were acquired (HNCO, HN(CA)CO, HNCA, HN(CO)CA, HNCACB, HN(CO)CACB) using non-uniform sampling (NUS) with a multi-dimensional Poisson Gap scheduling strategy with exponential weighting (*34*). NUS data were reconstructed using TopSpin3 and multidimensional decomposition (*35*). Backbone resonance assignments of the $Mg^{II}$-bound βPGM$_{D10N}$:P1G6P and

$Mg^{II}$-free βPGM$_{D10N}$:P1G6P complexes present simultaneously in the spectra were obtained using a simulated annealing algorithm employed by the *asstools* assignment program (*29*). Assignments for the two complexes were confirmed by using $^{1}H^{15}N$ TROSY spectra of separate $Mg^{II}$-bound and $Mg^{II}$-free $^{15}$N-βPGM$_{D10N}$:P1G6P complexes, together with sequential backbone amide to amide correlations obtained from TROSY-based (H)N(COCA)NNH and H(NCOCA)NNH experiments (*36*). The $Mg^{II}$-free $^{15}$N-βPGM$_{D10N}$:P1G6P complex was prepared by dilution of $Mg^{II}$ by over 20,000 fold using buffer exchange into standard NMR buffer in the absence of $MgCl_2$, while the $Mg^{II}$-bound $^{15}$N-βPGM$_{D10N}$:P1G6P complex was prepared in standard NMR buffer containing 50 mM $MgCl_2$.

**Determination of the $Mg^{II}$ dissociation constant.** A $Mg^{II}$-free $^{15}$N-βPGM$_{D10N}$:βG16BP complex was prepared from a reconstituted $Mg^{II}$-bound $^{15}$N-βPGM$_{D10N}$:βG16BP complex by buffer exchange (3000-fold dilution) and overnight equilibration into standard NMR buffer. A discontinuous titration of 0 – 47.6 mM $MgCl_2$ into separate $Mg^{II}$-free $^{15}$N-βPGM$_{D10N}$:βG16BP samples with overnight equilibration was monitored by $^{1}H^{15}N$ TROSY spectra recorded using a Bruker 800 MHz Avance I spectrometer equipped with a TXI probe and z-axis gradients (MBB). Peak intensities for well-resolved resonances of the $Mg^{II}$-bound βPGM$_{D10N}$:βG16BP complex (residues N10, G11, A115, K117 and I150) were averaged and normalized against the intensity of the sidechain Nε1 resonance of W216, which remains unchanged throughout the titration. The dissociation constant ($K_d$) was obtained by fitting changes in normalized peak intensity as a function of $Mg^{II}$ concentration to a single-site binding isotherm (*37*) using a non-linear least squares fitting algorithm. The solution concentration of $Mg^{II}$ present at the beginning of the titration was derived from the fitting procedure.

**X-ray crystallography.**

**Crystallization and data collection.** Frozen aliquots of substrate-free $\beta PGM_{D10N}$ or co-purified $\beta PGM_{D10N}$:βG16BP complex in standard native buffer (50 mM $K^+$ HEPES (pH 7.2), 5 mM $MgCl_2$, 2 mM $NaN_3$) were thawed on ice and centrifuged briefly to pellet insoluble material. Specific ligands were added to a solution of substrate-free $\beta PGM_{D10N}$ to generate crystals of the following complexes: $\beta PGM_{D10N}$:$BeF_3$ complex (5 mM $BeCl_2$ and 15 mM NaF), $\beta PGM_{D10N}$:P1G6P and $\beta PGM_{D10N}$:P6G1P complexes (15 mM βG1P, 5 mM $BeCl_2$ and 15 mM NaF) and $\beta PGM_{D10N}$:$AlF_4$:G6P complex (10 mM G6P, 5 mM $AlCl_3$ and 20 mM NaF). Crystals of the $\beta PGM_{D10N}$:$AlF_4$:$H_2O$:βG1P complex were obtained from a solution of the co-purified $\beta PGM_{D10N}$:βG16BP complexes containing 5 mM βG1P, 2 mM $AlCl_3$ and 10 mM $NH_4F$. Crystals of the co-purified $\beta PGM_{D10N}$:P1G6P complex were obtained from a solution of the co-purified $\beta PGM_{D10N}$:βG16BP complexes. The solutions were adjusted to a protein concentration of 0.6 mM, were incubated for 1 h and mixed 1:1 with precipitant (24 – 34% (w/v) PEG 4000 or 19 – 21% (w/v) PEG 3350, 50 − 200 mM Na acetate and 0 − 100 mM Tris (pH 7.5)). Crystals were grown at 290 K by hanging-drop vapor diffusion using a 2 μL drop suspended on a siliconized glass cover slip above a 700 μL well. Thin plate, small needle or rod shaped crystals grew typically over several days. Crystals were harvested using a mounted LithoLoop (Molecular Dimensions Ltd.) and were either cryo-protected in their mother liquor containing an additional 25% (v/v) ethylene glycol or excess mother liquor was removed (*38*) prior to plunging into liquid nitrogen. Diffraction data were collected at 100 K on the MX beamlines at the Diamond Light Source (DLS), Oxfordshire, United Kingdom and on beamline ID14-2 at the European Synchrotron Radiation Facility (ESRF), Grenoble, France.

**Data processing, structural determination and refinement.** At the DLS, data were processed using the xia2 pipeline (*39*), whereas at the ESRF, data were processed with

iMOSFLM (*40*). Resolution cut-offs were applied using either CC-half or by consideration of the $\langle I/\sigma(I)\rangle$ and $R_{merge}$ values. All the crystals belonged to the spacegroup $P2_12_12_1$, with cell dimensions that varied depending on the degree of enzyme closure. Structures were determined by molecular replacement with MolRep (*41*) using the highest resolution model with the most appropriate cap and core domain relationship as a search model. Model building was carried out in COOT (*42*) with ligands not included until the final rounds of refinement using REFMAC5 (*43*) so that they could be built into unbiased difference Fourier maps. When structures were refined with down-weighted B-factor restraints, the B-factors of the ligands in the resulting structures were equivalent to those of the surrounding protein, suggesting that the degree of accuracy in the placement of the ligand atoms was equivalent to those of the protein atoms. Structures with a resolution better than 1.4 Å were refined with anisotropic B-factors. Structure validation was carried out in COOT and MolProbity (*44*). Superpositions were carried out using PyMOL (*45*), maps were generated using FFT (*46*), and domain movements were calculated using DynDom (*47*). Additional details for X-ray crystallography data collection, data processing and refinement are provided in Table S1 in the Supporting Information.

**Crystallization of the $\beta PGM_{D10N}$:P1G6P and the $\beta PGM_{D10N}$:P6G1P complexes.** Rod shaped crystals harvested after 1 week contained predominantly βG16BP in the $\beta PGM_{D10N}$ active site, with the 6-phosphate group located in the *proximal* site and the 1-phosphate group bound in the *distal* site ($\beta PGM_{D10N}$:P6G1P complex). After refinement, the ratio of 2Fo − Fc contour thresholds between the 1- and 6-phosphate groups (*ca*. 6σ and 5σ, respectively) did not correlate with a full βG16BP ligand occupancy in the $\beta PGM_{D10N}$:P6G1P complex. When modeled at a ligand occupancy of 0.8, B-factor convergence was attained between the βG16BP ligand and neighboring residues in the active site, confirming βG16BP as the dominant ligand.

Remaining difference map peaks were consistent with the presence of a minor population of βG1P (with the 1-phosphate in the *distal* site) but, due to poor connectivity at this resolution, βG1P was not modeled into the structure. Crystals from the same drop with the same morphology harvested after 12 weeks contained only βG16BP bound in the alternate orientation with the 1-phosphate group located in the *proximal* site and the 6-phosphate group bound in the *distal* site ($\beta PGM_{D10N}$:P1G6P complex).

**Steady-state kinetic assays.** Steady-state kinetic assays for $\beta PGM_{WT}$ and substrate-free $\beta PGM_{D10N}$ were conducted at 294 K using a FLUOstar OMEGA microplate reader (BMG Labtech) in 200 mM $K^+$ HEPES buffer (pH 7.2) containing 5 mM $MgCl_2$ and 1 mM $NaN_3$ in a 200 µL reaction volume. The rate of G6P production was measured indirectly using a glucose 6-phosphate dehydrogenase (G6PDH) coupled assay, in which G6P is oxidized and concomitant $NAD^+$ reduction is monitored by the increase in absorbance at 340 nm (NADH extinction coefficient = 6220 $M^{-1}$ $cm^{-1}$). $\beta PGM_{WT}$ and substrate-free $\beta PGM_{D10N}$ stock concentrations were determined using a NanoDrop One$^C$ spectrophotometer (Thermo Scientific) and diluted accordingly (βPGM extinction coefficient = 19940 $M^{-1}$ $cm^{-1}$). For the determination of $k_{cat}$ and $K_m$ values, the reaction was initiated by the addition of 10 mM AcP to solutions of 0.5 mM $NAD^+$ and 5 units $mL^{-1}$ G6PDH containing either 5 nM $\beta PGM_{WT}$ or 500 nM substrate-free $\beta PGM_{D10N}$ and variable concentrations of βG1P (5, 15, 35, 50, 70, 100, 160, 230, 330 µM). The linear steady-state portion of G6P production was fitted using a linear least-squares fitting algorithm to determine the reaction velocity (v) at each βG1P concentration. Data were subsequently fitted to the standard Michaelis-Menten equation to derive $k_{cat}$ and $K_m$ values using an in-house python non-linear least-squares fitting algorithm. Errors were estimated using a python bootstrap resampling protocol and are presented at one standard deviation. For the

fluoride inhibition experiments monitored using the G6PDH coupled assay, the reaction was initiated by the addition of 10 mM AcP to solutions of 230 μM βG1P, 0.5 mM $NAD^+$ and 5 units $mL^{-1}$ G6PDH containing either 5 nM $\beta PGM_{WT}$ or 500 nM substrate-free $\beta PGM_{D10N}$ and variable concentrations of NaF (0, 1, 2, 3, 5, 7, 10 mM). The linear steady-state portion of G6P production was not used for the analysis of fluoride inhibition as βG16BP formation during the reaction outcompetes fluoride inhibition (*21*). The presence of increasing levels of fluoride in the reaction buffer extends the lag phase prior to achieving steady-state kinetics, the duration of which was estimated using a first derivative approach. The time point at which the maximum value was reached in the first derivative *vs* time plot for each reaction containing fluoride was normalized against the time point for the reaction in the absence of fluoride. A line of best fit for the normalized values *vs* fluoride concentration was determined using a polynomial function.

## RESULTS

**Recombinant $\beta PGM_{D10N}$ co-purifies in complex with βG16BP.** $\beta PGM_{D10N}$ was produced and purified as for $\beta PGM_{WT}$ with slight modifications to published procedures (*48*−*50*). A $^{31}P$ NMR spectrum demonstrated that, unlike $\beta PGM_{WT}$, $\beta PGM_{D10N}$ co-purifies with tightly-bound phosphorylated glucose ligands (Figure 2A). Four $^{31}P$ resonances are observed, two with chemical shifts corresponding to a 1-phosphate group and two to a 6-phosphate group of glucose. The ratio of intensities of the resonances suggests that the phosphate groups are paired, consistent with the population of two complexes. Ligand extraction was achieved by the removal of heat denatured $\beta PGM_{D10N}$ (2 min at 80 °C) using centrifugation followed by membrane filtration of the supernatant. $^{31}P$ and $^{1}H^{13}C$ HSQC NMR spectra indicated that a single ligand had

been isolated, which revealed that both complexes contained the same phosphorylated glucose species (Figure S1 A, C and D and Figure S2B in the Supporting Information). The ligand was identified as βG16BP (the reaction intermediate, Figure 1A) by comparison with synthetic α-and β-glucose 1,6-bisphosphate species (Figure S1E and Figure S2A). The high affinity of $\beta PGM_{D10N}$ for the βG16BP intermediate is predictable, since kinetic data for $\beta PGM_{WT}$ has identified that βG16BP is the tightest binding species of the native substrates, with $K_m$ = 0.63 μM (*8*) and $K_m$ = 0.72 μM (*30*). Substitution of aspartate with asparagine at residue 10 is likely to increase the binding affinity of $\beta PGM_{D10N}$ for βG16BP since the deprotonated D10 sidechain in $\beta PGM_{WT}$ does not satisfy charge balance (*24*) within the complex. Substrate-free $\beta PGM_{D10N}$ was prepared from the co-purified $\beta PGM_{D10N}$:βG16BP complexes by unfolding the recombinant protein in 4 M guanidine hydrochloride together with a 200-fold dilution of the ligand using buffer exchange and subsequent refolding of $\beta PGM_{D10N}$ (Figure S1B). A comparison of the $^{1}H^{15}N$ TROSY spectra of substrate-free $\beta PGM_{D10N}$ and $\beta PGM_{WT}$ indicated that $\beta PGM_{D10N}$ adopts a native conformation following refolding (Figure S3A).

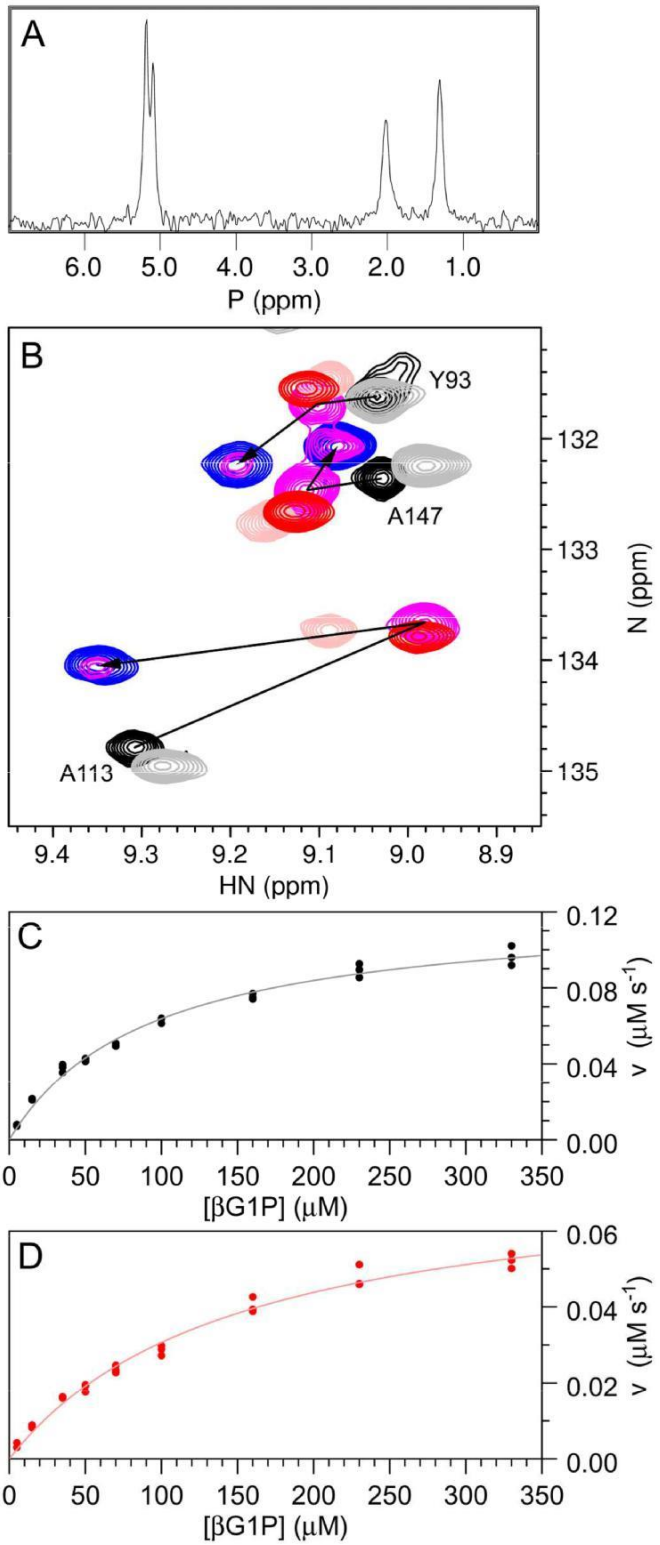
A
6.0
5.0
4.0
3.0
2.0
1.0
P (ppm)
B
Y93
A147
A113
132
133
134
135
N (ppm)
9.4
9.3
9.2
9.1
9.0
8.9
HN (ppm)
C
0.12
0.08
0.04
0.00
v (μM s-1)
0
50
100
150
200
250
300
350
[βG1P] (μM)
D
0.06
0.04
0.02
0.00
v (μM s-1)
0
50
100
150
200
250
300
350
[βG1P] (μM)

**Figure 2.** NMR spectra and reaction kinetics of $\beta PGM_{D10N}$. (A) $^{31}P$ spectrum of $\beta PGM_{D10N}$ immediately following purification showing four $^{31}P$ peaks (5.17, 5.08, 2.01 and 1.30 ppm) (ratio 6:5). Resonances at ~5 ppm and 1−2 ppm correspond to 6-phosphate and 1-phosphate groups of βG16BP, respectively. (B) Overlay of a section of $^{1}H^{15}N$ TROSY spectra for a range of $\beta PGM_{D10N}$ complexes: (black) substrate-free $\beta PGM_{D10N}$; (pink) $\beta PGM_{D10N}$:$BeF_3$ complex; (red) $\beta PGM_{D10N}{}^{P}$ – $^{1}H^{15}N$ BEST-TROSY spectrum started 6 min after addition of 20 mM AcP to substrate-free $\beta PGM_{D10N}$; (gray) substrate-free $\beta PGM_{D10N}$ – $^{1}H^{15}N$ BEST-TROSY spectrum started after a further 92 min by which time AcP has been depleted and $\beta PGM_{D10N}{}^{P}$ has reverted to substrate-free $\beta PGM_{D10N}$ (the small shift in peak positions is caused by an increase in inorganic phosphate concentration); (magenta) $\beta PGM_{D10N}{}^{P}$ as major species – $^{1}H^{15}N$ BEST-TROSY spectrum started 6 min after addition of 10 mM G6P and 20 mM AcP to substrate-free $\beta PGM_{D10N}$; (blue) $\beta PGM_{D10N}$:βG16BP complexes – $^{1}H^{15}N$ BEST-TROSY spectrum started after a further 145 min by which time AcP has been depleted and the $\beta PGM_{D10N}$:βG16BP complexes dominate in solution. The arrows indicate progression for the assigned residues from (black) substrate-free $\beta PGM_{D10N}$ to (magenta) $\beta PGM_{D10N}{}^{P}$ to (blue) the $\beta PGM_{D10N}$:βG16BP complexes. (C and D) Michaelis-Menten plots showing the dependence of the reaction velocity (v) for 5 nM $\beta PGM_{WT}$ (black circles; n=3) and 500 nM substrate-free $\beta PGM_{D10N}$ (red circles; n=3) on the initial βG1P concentration, monitored using a glucose 6-phosphate dehydrogenase coupled assay. Data were fitted to the standard Michaelis-Menten equation to derive $k_{cat}$ and $K_m$ values and the line of best fit is shown for $\beta PGM_{WT}$ (gray) and substrate-free $\beta PGM_{D10N}$ (pink).

**Substrate-free βPGM$_{D10N}$ readily forms a transient phospho-enzyme.** βPGM$_{WT}$ can be phosphorylated to generate βPGM$_{WT}^{P}$ by a number of priming agents, including not only βG16BP (Figure 1A) but also αG16BP, G6P, and acetyl phosphate (AcP) (*17*, *30*). In order to establish whether βPGM$_{D10N}$ could be similarly phosphorylated, incubation of 1 mM substrate-free βPGM$_{D10N}$ with 20 mM AcP was followed using a time course of $^{1}H^{15}N$ BEST-TROSY spectra (*32*, *33*) with 6 min time resolution (Figure 2B). The initial spectra overlaid closely with a $^{1}H^{15}N$ TROSY spectrum of the βPGM$_{D10N}^{P}$ complex, which is an analogue of βPGM$_{D10N}$ prepared using conditions described previously for the βPGM$_{WT}$:$BeF_3$ complex (Figure S3B) (*23*). This established that βPGM$_{D10N}^{P}$ is generated during the 6 min dead-time of the time course. After 98 min, the $^{1}H^{15}N$ BEST-TROSY spectrum had reverted entirely to that of substrate-free βPGM$_{D10N}$. Monitoring the same reaction using $^{31}P$ NMR spectra, the hydrolysis rate constant for βPGM$_{D10N}^{P}$ was determined to be 0.020 ± 0.002 $s^{-1}$ (Figure S3C). The equivalent rate constant for βPGM$_{WT}^{P}$ under the same conditions is only 3 fold greater (0.060 ± 0.006 $s^{-1}$), indicating that the proposed general acid-base (D10) has little involvement in the attack of βPGM$^{P}$ by water. Attempts to crystallize the meta-stable species βPGM$_{D10N}^{P}$ were unsuccessful. However, the βPGM$_{D10N}$:$BeF_3$ complex was crystallized and the structure was determined to 1.3 Å resolution (PDB 5OJZ; Figure 3 A and G, Figure S4A and Table S1). The cap and core domains were in a predominantly open conformation, as in the βPGM$_{WT}$:$BeF_3$ complex (PDB 2WFA (*23*); non-H atom RMSD = 1.06 Å), and the sidechain of residue N10 was in the *out* position (Figure 1B), thereby not positioned to contribute to the nucleophilic attack of βPGM$_{D10N}^{P}$ by water. The close similarity of $^{1}H^{15}N$ TROSY spectra between βPGM$_{WT}$:$BeF_3$,

βPGM$_{D10N}$:BeF$_3$ and βPGM$_{D10N}^{P}$ indicates that these structural features are common to all three species in solution.

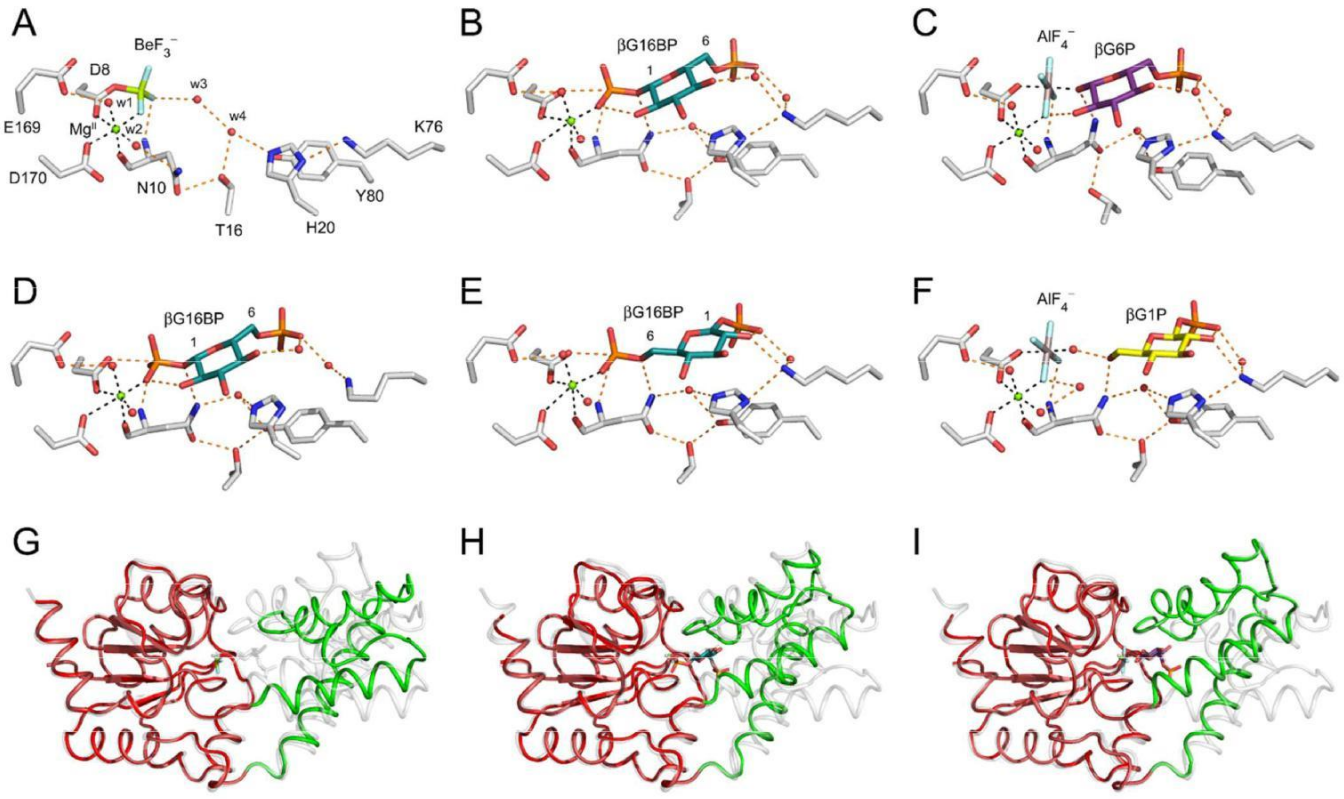


**Figure 3.** Overviews of the active sites and the extent of domain closure in the βPGM$_{D10N}$ complexes. The active sites of (A) βPGM$_{D10N}$:BeF$_3$ complex (PDB 5OJZ), (B) βPGM$_{D10N}$:P1G6P complex (PDB 5OK1), (C) βPGM$_{D10N}$:AlF$_4$:G6P complex (PDB 5OK2), (D) co-purified βPGM$_{D10N}$:P1G6P complex (PDB 5O6P), (E) βPGM$_{D10N}$:P6G1P complex (PDB 5OK0) and (F) βPGM$_{D10N}$:AlF$_4$:H$_2$O:βG1P complex (PDB 5O6R). Selected active site residues and ligands are shown as sticks in standard CPK colors, with beryllium (light green), fluorine (light blue), aluminum (dark gray), βG16BP (teal carbon atoms; with C1 and C6 labeled for clarity), G6P (purple carbon atoms) and βG1P (gold carbon atoms). Structural waters (red) and

the catalytic $Mg^{II}$ ion (green) are drawn as spheres. Orange dashes indicate hydrogen bonds and black dashes show metal ion coordination. The extent of domain closure is shown in (G) $\beta PGM_{D10N}$:$BeF_3$ complex (PDB 5OJZ), (H) $\beta PGM_{D10N}$:P1G6P complex (PDB 5OK1) and (I) $\beta PGM_{D10N}$:$AlF_4$:G6P complex (PDB 5OK2). The protein backbone of $\beta PGM_{D10N}$ is depicted as a ribbon, with the core (red) and the cap (green) domains indicated and the ligands shown as sticks and spheres (colored as above). The pale gray ribbons indicate the open $\beta PGM_{WT}$ structure (PDB 2WHE (*20*)) and the fully closed $\beta PGM_{WT}$:$MgF_3$:G6P TSA complex (PDB 2WF5 (*20*)) superposed on the core domains to show the extent of domain closure in the $\beta PGM_{D10N}$ complexes.

**The substrate-free $\beta PGM_{D10N}$ preparation has mutase activity.** In addition to substrate-free $\beta PGM_{D10N}$ having similar levels of phosphatase activity to $\beta PGM_{WT}$, the substrate-free $\beta PGM_{D10N}$ preparation was also found to have mutase activity. The standard glucose 6-phosphate dehydrogenase coupled assay (*8*, *17*, *18*) was used to monitor conversion of βG1P to G6P using AcP as the priming agent. The kinetic profile displayed the characteristic lag phase for βPGM (Figure S3 I and J) (*30*), and a simple steady-state Michaelis-Menten analysis of the linear portion (Figure 2D), yielded values for $k_{cat}$ of 0.15 ± 0.01 $s^{-1}$ and $K_m$ of 150 ± 12 μM. Measurements under the same conditions for $\beta PGM_{WT}$ (Figure 2C), yielded values of 24.5 ± 0.7 $s^{-1}$ and 92 ± 6 μM, respectively; minor levels of inhibition by the priming agent (*17*, *30*) is a likely source of the slightly different values determined here compared with some reported previously for $\beta PGM_{WT}$ (*8*, *30*). Contaminating *E. coli* $\beta PGM_{WT}$ is unlikely to be the source of mutase activity in the substrate-free $\beta PGM_{D10N}$ preparation as there is no equilibration of βG1P

with G6P over a similar timeframe by $\beta PGM_{D8N}$ (Figure S3D), which has identical chromatography retention characteristics to $\beta PGM_{D10N}$. To investigate whether the activity of the substrate-free $\beta PGM_{D10N}$ preparation was the result of recovery by acetate (derived from AcP hydrolysis) substituting for the general acid-base, the equilibration of βG1P with G6P was primed with βG16BP rather than AcP (Figure S3E). Mutase activity was again observed (with a slightly larger rate constant, $k_{cat} = 0.6\ s^{-1}$, as there is no inhibition when βG16BP is used as the priming agent) and thus acetate was not playing a significant role in recovery of activity. In contrast, it has not been possible to eliminate low levels (~ 0.6%) of contaminating *L. lactis* $\beta PGM_{WT}$ as the source of mutase activity because the measured $K_m$ values, and degree of inhibition by inorganic phosphate (Figure S3F), and by fluoride (Figure S3G) are not sufficiently different between the substrate-free $\beta PGM_{D10N}$ preparation and $\beta PGM_{WT}$. Low levels of $\beta PGM_{WT}$ can potentially be formed by translational mis-incorporation or by deamidation of $\beta PGM_{D10N}$ during refolding, where the N10-G11 sequence will have elevated susceptibility (*51*). However, it is difficult to rationalize the dominant effect arising either from translational mis-incorporation, when an increase in mutase activity is observed following βG16BP removal ($k_{cat}$ = 0.002 $s^{-1}$ for co-purified $\beta PGM_{D10N}$ *vs* $k_{cat}$ = 0.2 $s^{-1}$ for the substrate-free $\beta PGM_{D10N}$ preparation), or from deamidation, when only a 2-fold increase in activity is observed following 2 h *vs* 48 h incubation with 4 M guanidine hydrochloride prior to refolding (Figure S3 K and L).

**Substrate-free $\beta PGM_{D10N}$ slowly reforms stable βG16BP complexes.** In order to establish that the substrate-free $\beta PGM_{D10N}$ preparation was capable of reconstituting the $\beta PGM_{D10N}$:βG16BP complexes *in situ*, the equilibration of 10 mM βG1P with G6P (and *vice*

*versa*) by 1 mM substrate-free βPGM$_{D10N}$ in the presence of 20 mM AcP was monitored using a time course of $^{1}H^{15}N$ BEST-TROSY spectra with 6 min time resolution (Figure 2B). At this concentration of substrate-free βPGM$_{D10N}$, βG1P and G6P were fully equilibrated (*via* βG16BP, Figure 1A) in the 6 min dead-time of the time course, and the initial enzyme species observed was βPGM$_{D10N}^{P}$. βPGM$_{D10N}^{P}$ was slowly replaced ($k_{obs} = 5 \times 10^{-4}$ $s^{-1}$) by two conformationally distinct species (Figure S5), that reproduce the $^{31}P$ NMR spectrum of the co-purified βPGM$_{D10N}$:βG16BP complexes (Figure 2A). When 20 mM AcP and 10 mM βG1P were added to the reconstituted βPGM$_{D10N}$:βG16BP complex preparation, the rate constant of equilibration was within error of that of the original substrate-free βPGM$_{D10N}$ preparation (Figure S3H).

**The nucleophile in the βPGM$_{D10N}$:P1G6P complex is aligned for attack.** The βPGM$_{D10N}$:βG16BP complexes were explored using X-ray crystallography to compare their structures with those of metal fluoride analogue complexes (*19*, *20*, *23*). A reconstituted βPGM$_{D10N}$:βG16BP complex was crystallized and the structure was determined to 1.9 Å resolution (PDB 5OK1; Figure 3 B and H, Figure S4B and Table S1). In this structure, βG16BP is bound in a single orientation, with the 1-phosphate in the *proximal* site and the 6-phosphate in the *distal* site, and is hence termed the βPGM$_{D10N}$:P1G6P complex. This structure mimics the active site conformation immediately preceding phosphoryl transfer from βG16BP to βPGM in Step 2 (Figure 1A). This conformation requires a protonated general acid-base and its surrogate, N10, forms a hydrogen bond through its sidechain amide group to the bridging oxygen of the 1-phosphate of βG16BP. The 1-phosphorus atom is positioned in-line for attack by D8 atom Oδ1 (O − P − O angle = 170$^{o}$) with a donor-acceptor oxygen atom separation of 4.6 Å and a nucleophile-phosphorus distance of 3.0 Å, which is inside the sum of the van der Waals radii for

these two atoms (3.3 Å) (Figure 3B) (*52*). The donor-acceptor oxygen atom separation is larger than is observed in TSA complexes containing $AlF_4^-$ (3.9 Å; PDB 2WF6) and $MgF_3^-$ (4.3 Å; PDB 2WF5 (*20*)) and in some DFT models of the TS for this chemical step in $\beta PGM_{WT}$, (4.2 Å (*11*); 4.4 Å (*12*)). A co-purified $\beta PGM_{D10N}$:βG16BP complex was also crystallized and the structure was determined to 2.2 Å resolution (PDB 5O6P; Figure 3D, Figure S4C and Table S1). In this structure, βG16BP is bound in the same orientation as that present in the reconstituted $\beta PGM_{D10N}$:P1G6P complex and the two complexes overlay closely with a non-H atom RMSD = 0.43 Å (Figure S6 and Table S2). The active site arrangement present in both $\beta PGM_{D10N}$:P1G6P complexes conforms to the definition of an aligned NAC (*23*, *26*), where atomic distances and geometries lie close to those of TS models (*25*). Given the close similarity between the complexes, the structure of the reconstituted $\beta PGM_{D10N}$:βG16BP complex will be used in the comparisons described below.

**The $\beta PGM_{D10N}$:P1G6P complex is not fully closed.** In contrast to all deposited metal fluoride analogue βPGM structures, the alignment of the nucleophile in the $\beta PGM_{D10N}$:P1G6P complex is satisfied without full closure of the enzyme (Figure 3 B and H and Table S2). Compared to the $\beta PGM_{WT}$:$MgF_3$:G6P TSA complex (PDB 2WF5 (*20*)), the relative orientation of the cap and core domains undergoes a rotation of $13^o$, and there are significant changes in the hydrogen bonding network within the vicinity of the general acid-base residue. N10 donates a hydrogen bond to βG16BP (through atom Nδ2), while simultaneously accepting a hydrogen bond (through atom Oδ1) from the backbone amide NH and the sidechain OH groups of T16. Crucially, residue T16 dictates the relative degree of closure of the cap and core domains (*8*, *23*), and in the $\beta PGM_{D10N}$:P1G6P complex the conformation of T16 is near the midpoint of the

transition between the substrate-free βPGM$_{WT}$ and the βPGM$_{WT}$:MgF$_3$:G6P TSA structures. The inference is that van der Waals contact between the attacking nucleophile and the 1-phosphorus atom of βG16BP in the βPGM$_{D10N}$:P1G6P complex, resists a donor-acceptor oxygen atom separation of less than 4.6 Å, the effect of which propagates through the structure to prevent the TS hydrogen bonding organization and full domain closure from being established (*11*−*13*, *20*). Moreover, asymmetrical electron density for the catalytic $Mg^{II}$ ion in the βPGM$_{D10N}$:P1G6P complex shows clear evidence of a deviation from optimal octahedral coordination geometry (Figure S7A), with elongation of distances and distortion of angles, that is not observed in metal fluoride-based ground and transition state analogue complexes of βPGM. This result implies that a competition exists in $Mg^{II}$ ion coordination between the oxygen atom of the 1-phosphate group of βG16BP (O – $Mg^{II}$ = 2.0 Å) and the carboxylate oxyanion of residue D170 (O – $Mg^{II}$ = 2.6 Å). The equilibrium position of the $Mg^{II}$ ion lies towards coordination by the phosphate oxygen atom, which is expected to have a higher anionic charge density, with subsequent compromising of coordination by enzymatic oxygen and oxyanion ligands. Together, these observations illustrate the interdependency between donor and acceptor atom separation, optimal hydrogen bond organization, optimal catalytic $Mg^{II}$ ion coordination, and full domain closure to achieve TS architecture.

**The βPGM$_{D10N}$:AlF$_4$:G6P TSA complex is fully closed.** In order to establish that the antagonism of full closure in the βPGM$_{D10N}$:P1G6P complex was not simply an artefact of the aspartate to asparagine substitution, the βPGM$_{D10N}$:AlF$_4$:G6P TSA complex was crystallized and the structure was determined to 1.1 Å resolution (PDB 5OK2; Figure 3 C and I, Figure S4D and Table S1). This complex superimposes very closely with the βPGM$_{WT}$:AlF$_4$:G6P TSA complex

(PDB 2WF6; non-H atom RMSD = 0.13 Å) and it binds G6P with the 6-phosphate in the *distal* site and the square planar $AlF_4^-$ moiety mimicking the transferring phosphoryl group in the *proximal* site between D8 (atom Oδ1) and the 1-OH group of G6P (*53*). The donor-acceptor distance and angle of alignment are identical to those in the $\beta PGM_{WT}$:$AlF_4$:G6P TSA complex (3.8 Å and 173°, respectively). However, a comparison of the hydrogen bonding arrangements between D10/N10 and the 1-oxygen of G6P in the $\beta PGM_{WT}$:$AlF_4$:G6P TSA and the $\beta PGM_{D10N}$:$AlF_4$:G6P TSA complexes reveals a difference in the identity of the proton donor and proton acceptor. Whereas in the $\beta PGM_{WT}$:$AlF_4$:G6P TSA complex, the transferring proton is bonded to the 1-OH group of G6P and is coordinated by the anionic carboxylate group of the general acid-base, the analogous hydrogen bond in the $\beta PGM_{D10N}$:$AlF_4$:G6P TSA complex has the sidechain $NH_2$ group of N10 coordinated by what is likely to be the deprotonated 1-oxygen of G6P. Owing to the ability of the active site to accommodate the D10 to N10 substitution, the $\beta PGM_{D10N}$ variant is capable of full domain closure with concomitant formation of TS geometry.

**The $\beta PGM_{D10N}$:P6G1P complex closely resembles the $\beta PGM_{D10N}$:P1G6P complex.** While crystals harvested after 12 weeks consisted exclusively of the $\beta PGM_{D10N}$:P1G6P complex, a crystal with the same morphology harvested from the same drop after only 1 week yielded a 2.2 Å resolution structure of a different complex. While the resolution of the structure was limited, the electron density clearly showed that the structure contained βG16BP bound in the alternate orientation, with the 6-phosphate in the *proximal* site and the 1-phosphate in the *distal* site, and is hence termed the $\beta PGM_{D10N}$:P6G1P complex (PDB 5OK0; Figure 3E, Figure S4E and Table S1). Overall, the orientation of βG16BP does not have a strong influence on the degree of domain closure in the $\beta PGM_{D10N}$:βG16BP complexes (non-H atom RMSD = 0.34 Å). The

relative orientation of the cap and core domains compared to the βPGM$_{D10N}$:AlF$_4$:G6P TSA complex have rotations of 13$^o$ (βPGM$_{D10N}$:P1G6P) and 14$^o$ (βPGM$_{D10N}$:P6G1P) (Table S2). The βPGM$_{D10N}$:P6G1P complex can again be defined as an aligned NAC (O − P − O angle = 176$^o$, a donor-acceptor oxygen atom separation of 4.7 Å and a nucleophile-phosphorus distance of 3.1 Å) and the hydrogen bonding of residue N10 is analogous to that present in the βPGM$_{D10N}$:P1G6P complex. There is also a direct hydrogen bond present between the sidechain OH group of S52 and the 3-OH group of βG16BP in the βPGM$_{D10N}$:P6G1P complex, whereas in the βPGM$_{D10N}$:P1G6P complex, hydrogen bonding between βG16BP and the protein is mediated by two water molecules (Figure S8), as observed previously in TSA complexes involving G6P and β-glucose 1-phosphonates (*19*). Hence, alignment of the βG16BP intermediate is achieved in both βPGM$_{D10N}$:βG16BP complexes without full closure of the enzyme.

**The βPGM$_{D10N}$:AlF$_4$:H$_2$O:βG1P complex is partially open.** The structure of the βPGM$_{D10N}$:AlF$_4$:βG1P complex was investigated to ascertain if it behaved analogously to the βPGM$_{D10N}$:AlF$_4$:G6P TSA complex, thus providing a direct comparator for the βPGM$_{D10N}$:P6G1P complex. The crystal structure of the βPGM$_{D10N}$:AlF$_4$:βG1P complex was determined to 1.4 Å resolution (PDB 5O6R; Figure 3F, Figure S4F and Table S1). Surprisingly, the structure did not resemble that of the fully closed βPGM$_{WT}$:AlF$_4$:G6P TSA complex (PDB 2WF6), but instead the protein atoms superimposed almost exactly with the partially open βPGM$_{D10N}$:P6G1P complex (non-H atom RMSD = 0.33 Å). Uniquely in βPGM structures, electron density consistent with a water molecule occupying an axial ligand position of the $AlF_4^-$ moiety (instead of the 6-oxygen of βG1P) was present, with D8 still occupying the other axial

position, and this structure is hence termed a βPGM$_{D10N}$:AlF$_4$:H$_2$O:βG1P complex. The water molecule satisfies the demands of the $AlF_4^-$ moiety for octahedral coordination while allowing the cap domain and hydrogen bonding pattern between N10, T16 and D15 to adopt that of the βPGM$_{D10N}$:P6G1P complex. The sidechain $NH_2$ group of N10 remains hydrogen bonded to the 6-OH group of βG1P rather than switching to the water molecule, despite the 6-OH group of βG1P being located further from D8 (6-OH − Oδ1 = 5.7 Å), compared with the 6-oxygen of βG16BP in the βPGM$_{D10N}$:P6G1P structure (6-O – Oδ1 = 4.6 Å). This structure implies that there is greater resistance to the formation of the fully closed βPGM$_{D10N}$:$AlF_4^-$ TSA complex with βG1P than with G6P. In contrast to the apparent deprotonation of the 1-oxygen of G6P in the βPGM$_{D10N}$:AlF$_4$:G6P TSA complex, deprotonation of the 6-OH group of βG1P appears not to be the preferred arrangement in the βPGM$_{D10N}$:AlF$_4$:βG1P complex, correlating with the ~3 unit difference in solution p$K_a$ values for the two hydroxyl groups (*54*).

**The βPGM$_{D10N}$:P1G6P complex dominates in solution.** The crystal structures of the βPGM$_{D10N}$:βG16BP complexes with the intermediate bound in the two orientations presents a rationale for the non-equivalent complexes observed in solution using $^{31}P$ and $^{1}H^{15}N$ TROSY NMR approaches (Figure 2A and Figure S5). In the βPGM$_{D10N}$:P1G6P complex (Figure 3B), there is close proximity between H4 of βG16BP and the imidazole group of residue H20, which should result in a marked upfield chemical shift change of the H4 resonance through aromatic ring current effects. In the βPGM$_{D10N}$:P6G1P complex (Figure 3E), this chemical shift change should instead be experienced by the H3 resonance because of the change in orientation of the βG16BP ligand. To investigate the two βPGM$_{D10N}$:βG16BP complexes in solution, $^{1}H^{13}C$ HSQC

and CCH-TOCSY spectra were acquired using 1:1 $\beta PGM_{D10N}$ and 100% U-$^{13}$C-βG16BP (Figure S2C). In both $\beta PGM_{D10N}$:βG16BP complexes only the H4 resonance of βG16BP is shifted markedly upfield on binding ($\Delta\delta$ = 1.05 and 1.18 ppm), while the H3 resonance of βG16BP is shifted slightly downfield ($\Delta\delta$ = 0.08 and 0.14 ppm). Together, these results indicate that the bound orientation of βG16BP is the same in the two solution forms, thus identifying both as $\beta PGM_{D10N}$:P1G6P complexes. The dominance of $\beta PGM_{D10N}$:P1G6P over $\beta PGM_{D10N}$:P6G1P complexes in solution mirrors the relative dissociation constants for G6P (9 μM) and βG1P (46 μM) in the $\beta PGM_{WT}$:$AlF_4^-$ TSA complexes (*19*).

**The $\beta PGM_{D10N}$:P1G6P complex has weak $Mg^{II}$ affinity.** The source of the difference between the two solution $\beta PGM_{D10N}$:P1G6P complexes was investigated using NMR backbone resonance assignment. All 210 of the non-proline residues were assigned, of which 115 showed more than one spin system. No significant structural differences were identified upon calculation of dihedral angles using TALOS-N (*55*) (Figure S5 E and F). Residues with the largest chemical shift differences between the two complexes were principally located within the active site (Figure S5G). For $^{15}$N, these comprise L9 (−2.29 ppm), V47 (−2.15 ppm), V141 (−2.78 ppm) and D170 (−2.16 ppm), for $^{13}$C', N10 (−2.69 ppm) and D170 (−1.74 ppm), for $^{13}$Cα, D8 (0.81 ppm), N10 (−0.86 ppm) and S144 (−0.90 ppm), and for $^{13}$Cβ, K45 (−0.80 ppm) and S171 (−0.93 ppm) (Figure S5 A and B). Residues N10 and D170 are involved with the ligation of the catalytic $Mg^{II}$ ion, suggesting that changes in this coordination may be responsible for the chemical shift differences observed. To investigate, an $Mg^{II}$-free form of the $\beta PGM_{D10N}$:P1G6P complex was prepared and the $^1H^{15}N$-TROSY spectrum corresponded to one of the assigned $\beta PGM_{D10N}$:P1G6P complexes, while addition of $Mg^{II}$ resulted in the other. Overall, the backbone

chemical shift differences between the $Mg^{II}$-bound and $Mg^{II}$-free $\beta PGM_{D10N}$:P1G6P complexes are reminiscent of those between the $\beta PGM_{WT}$:$MgF_3$:G6P TSA complex (BMRB 7234 (*20*)) and the $Mg^{II}$-bound $\beta PGM_{D10N}$:P1G6P complex in terms of the residues involved, but are smaller in magnitude (Figure S5 C and D). Using changes in $^{1}H^{15}N$-TROSY peak intensities on addition of $Mg^{II}$ to the $Mg^{II}$-free $\beta PGM_{D10N}$:P1G6P complex, the dissociation constant for $Mg^{II}$ binding was determined to be 7.1 ± 0.6 mM (Figure S7 B and C), consistent with the initial purification of the $\beta PGM_{D10N}$:P1G6P complexes being a mixture of $Mg^{II}$-bound and $Mg^{II}$-free forms in the presence of 5 mM $MgCl_2$. In contrast, all metal fluoride analogue complexes of βPGM exist in solution as $Mg^{II}$-bound species at this concentration of $MgCl_2$. The changes in the $^{31}P$ NMR chemical shifts between the $Mg^{II}$-bound and $Mg^{II}$-free $\beta PGM_{D10N}$:P1G6P complexes (1-phosphate = +0.71 ppm, 6-phosphate = −0.09 ppm) are small compared with those associated with protonation of βG1P (−3.4 ppm) or G6P (−3.6 ppm) (Figure 2A and Figure S1 F−K), indicating that $Mg^{II}$ binding is not influenced significantly by protonation of either phosphate group. Rather, the surprisingly low affinity for $Mg^{II}$ at this point on the reaction coordinate correlates with its sub-optimal coordination geometry in the structure of the $\beta PGM_{D10N}$:P1G6P complex (Figure S7A), in contrast to the regular $Mg^{II}$ coordination geometry observed in the $\beta PGM_{D10N}$:$BeF_3$ and $\beta PGM_{D10N}$:$AlF_4$:G6P TSA complex structures.

## DISCUSSION

A unique behavior of the $\beta PGM_{D10N}$ variant is that, unlike all other forms of βPGM examined to date, it co-purifies as tight, non-covalently bound $\beta PGM_{D10N}$:βG16BP complexes. Effective removal of the bound βG16BP reaction intermediate required an unfolding-dilution-refolding

approach. When challenged with substrate in the presence of excess AcP, the substrate-free $\beta PGM_{D10N}$ preparation equilibrates βG1P and G6P, with $\beta PGM_{D10N}^{P}$ maintained as the primary enzyme species. On depletion of AcP, the enzyme population shifts slowly to the $\beta PGM_{D10N}$:P1G6P complex becoming the dominant species. In this complex, the 1-phosphate group of βG16BP is aligned with the carboxylate oxygen atom of D8, and the sidechain of N10 is shifted to the *in* position, where it forms a hydrogen bond with the bridging 1-oxygen atom of βG16BP. The enzyme is now caught in the act of phosphoryl transfer, geometrically close to the TS, but unable to complete the reaction (or at least overwhelmingly favoring the 1-phosphate group being bonded to G6P), as N10 will not release the proton hydrogen bonded to the bridging oxygen atom.

The DFT calculations of $\beta PGM_{WT}$ reflect enzymatic phosphoryl transfer reactions in general (*25*) in that the point at which proton transfer occurs is controversial. Two $\beta PGM_{WT}$ models predict that, when D8 attacks βG16BP in Step 2, proton transfer to βG16BP occurs prior to TS formation, and in the TS there is a donor to acceptor atom separation of 4.2 Å (*11*) or 4.4 Å (*12*). In a third model, proton transfer is synchronous with TS formation involving a donor to acceptor atom separation of 4.0 Å (*56*), while in a fourth model, proton transfer to βG16BP occurs after TS formation, and in the TS there is a donor to acceptor atom separation of 5.0 Å (*13*). The experiment supports the predictions of the first two models, as the $\beta PGM_{D10N}$:P1G6P complex rather than the $\beta PGM_{D10N}^{P}$:G6P complex is trapped and, without proton transfer, the donor to acceptor atom separation is held at 4.6 Å. Intriguingly, in the 4.4 Å TS model (*12*), a compression of the donor to acceptor atom separation to less than 4.6 Å is associated with the start of proton transfer from D10 to βG16BP. Moreover, with the donor to acceptor atom

separation being held 0.2 − 0.4 Å greater than that in the TS, the two domains of βPGM do not complete their closure. Full closure, including the hydrogen bonding of T16 and N10/D10 found in the TS, is only stable when there is compression of the reaction coordinate to below the van der Waals contact distance, as mimicked by the TSA complexes ($AlF_4^-$ = 3.9 Å, PDB 2WF6; $MgF_3^-$ = 4.3 Å, PDB 2WF5 (*20*)) (Figure 4). Corroboration of the partial closure of the $βPGM_{D10N}$ complexes is also present in the solution ensembles, where residues of the hinge in the $βPGM_{D10N}$:P1G6P complex lie in an intermediate position between the open and the TSA conformations, and residues D15 and T16 fail to achieve the hydrogen bond arrangement in the TS model (Figure S9). Together, these observations illustrate the complementarity between the TS and the optimal hydrogen bonding of the fully closed enzyme in the TSA conformation, as opposed to the partially open ground state βG16BP complex, and thus a means by which the enzyme discriminates between the TS (binding it tightly enough to have a sufficiently fast chemical step) and product (binding it weakly enough that it does not dissociate too slowly).

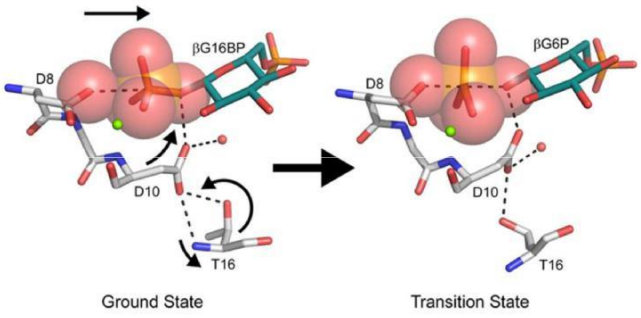


**Figure 4.** A schematic showing the conformational changes required for ground state to transition state progression in βPGM. Despite van der Waals contact between the attacking nucleophilic carboxylate oxygen atom of D8 and the 1-phosphorus atom of βG16BP in the

ground state βPGM$_{D10N}$:P1G6P complex (PDB 5OK1), the hydrogen bonding organization of the transition state is not attained. A shift in hydrogen bonding partners between T16 and D10 is required to allow positional changes in both sidechains, which delivers the protonated general acid-base to the bridging oxygen atom of βG16BP. Following proton transfer, further compression along the donor-acceptor oxygen atom trajectory occurs, establishing the conformation of the transition state (model derived from the βPGM$_{WT}$:MgF$_3$:G6P TSA complex; PDB 2WF5 (*20*)). Selected active site residues and ligands are shown as sticks in standard CPK colors, with a structural water (red) and the catalytic $Mg^{II}$ ion (green) drawn as spheres. Large translucent spheres represent van der Waals radii for the oxygen and phosphorus atoms of the transferring phosphoryl group.

The rate constant for hydrolysis of the phospho-enzyme is almost unaffected by the D10N mutation. This result is readily rationalized if hydrolysis occurs with residue 10 in the *out* position, as observed for N10 in the βPGM$_{D10N}$:BeF$_3$ complex (PDB 5OJZ) and D10 in the βPGM$_{WT}$:BeF$_3$ complex (PDB 2WFA (*23*)). Previously, it had been proposed that D10 was engaged in the hydrolysis reaction of βPGM$_{WT}^{P}$ on the basis of a rate acceleration by the mutated hinge variant βPGM$_{T16P}$ (*8*). However, this mechanism is not dominant in βPGM$_{WT}$; the water molecule that attacks the phosphate group during hydrolysis must at least as readily transfer a proton to an ancillary base as to residue 10. The identity of the ancillary base remains to be established but the oxygen atoms of the transferring phosphoryl group (*via* one or more water molecules) are strong local candidates. However, the base may be another residue in βPGM$_{WT}$ (except for residue H20 (*8*)) or the buffer, *via* extended hydrogen bonded networks involving multiple water molecules.

While the $\beta PGM_{D10N}{}^{P}$ hydrolysis rate constant cannot be rationalized by a contaminant within the substrate-free $\beta PGM_{D10N}$ preparation, $\beta PGM_{D10N}$ is not unequivocally the source of the observed mutase activity. However, similarly to the phospho-enzyme hydrolysis reaction, it is plausible that proton transfer to the incipient hydroxyl group of G6P or βG1P (as the 1- or 6-phosphoryl group of βG16BP transfers to residue D8) is delivered from an ancillary acid by a water molecule. In a model of the $\beta PGM_{D10N}$:P1G6P complex with N10 moved to the *out* position (Figure S10), the two water molecules that occupy the space vacated by the sidechain of N10 comprise part of an extended hydrogen bonded network, involving active site residues H20, K76, Y80 and the phosphate group in the *distal* site, and reaching to bulk solvent. Any one of these groups or the buffer (or even potentially the phosphate group in the *proximal* site) could act as the ancillary acid *via* one or more water molecules, allowing low level mutase activity to occur in $\beta PGM_{D10N}$.

Regardless of the source of the mutase activity, the replacement of D10 with N10 leads to at least a ~350 fold (Figure S3 I and J) reduction in activity. Consequently, the primary effect of introducing the general acid-base into $\beta PGM_{WT}$ is to elevate the rate of substrate turnover to ~$10^3$ fold (Figure S3 C and I) greater than the rate of phospho-enzyme hydrolysis, enabling the enzyme to discriminate reaction with substrate over reaction with water. This ensures that βPGM is primarily a mutase rather than a phosphatase.

The co-purified $\beta PGM_{D10N}$:βG16BP complexes are present as a near-equimolar mixture of $Mg^{II}$-bound and $Mg^{II}$-free $\beta PGM_{D10N}$:P1G6P complexes in standard NMR buffer (5 mM $Mg^{II}$).

This reflects the surprisingly low affinity of these complexes for $Mg^{II}$ ($K_d$ = 7.1 mM) compared with the apparent $K_m$ = 270 μM for $Mg^{II}$ in the reaction involving $\beta PGM_{WT}$ (*17*), and is similar to the physiological concentration of $Mg^{II}$ for *L. lactis* (~7 mM (*57*)). The conclusion is that βG16BP binding leads to a sub-optimally coordinated catalytic $Mg^{II}$ ion until full closure is achieved. More optimal coordination of the catalytic $Mg^{II}$ ion is found in structures that include the 0.2 − 0.4 Å reduction in donor to acceptor atom separation associated with the formation of experimental TSA complexes and in DFT models of the TS. In a different class of phosphoryl transfer enzymes, the catalytic $Mg^{II}$ ion has been identified to play a role in the rate of lid opening during the reaction cycle of adenylate kinase (*58*), as well as reducing non-productive active site fluctuations, stabilizing TS architecture, and serving as an anchor to stabilize the nucleophilic phosphate group. In βPGM, rather than acting as a pivot for opening, it appears that the catalytic $Mg^{II}$ ion is favoring TS binding and disfavoring substrate binding by forming a looser association with its ligands as the TS relaxes to ground state complexes.

## CONCLUSIONS

The employment of an aspartate to asparagine substitution of the assigned general acid-base of βPGM allowed the examination of stable enzyme:substrate complexes through the ability of $\beta PGM_{D10N}$ to trap the βG16BP reaction intermediate *in situ*. Unlike previous structures determined for substrate, transition state, and product analogue complexes involving βG1P and G6P, the βG16BP complex achieves both alignment and contact of the attacking nucleophile with its target but without full closure of the enzyme. This reveals the interplay between compression of the reaction coordinate to below the van der Waals contact distance and the

protein conformation that supports the transition state for the chemical step. The coordination of the catalytic $Mg^{II}$ ion is an important element of this interplay on the one hand by complementing the transition state and on the other by facilitating the release of the reaction intermediate on an appropriate timescale.

ASSOCIATED CONTENT

**Supporting Information**

The Supporting Information is available free of charge on the ACS Publications website at DOI:

$^{31}P$, $^{1}H^{13}C$ HSQC and $^{1}H^{15}N$ TROSY NMR spectra; βPGM reaction kinetics, electron density difference and omit maps for the $βPGM_{D10N}$ complexes; diagrams of chemical shift differences and backbone dihedral angles; superposition of the $βPGM_{D10N}$:P1G6P complexes; coordination and binding affinity of the catalytic $Mg^{II}$ ion in the $βPGM_{D10N}$:P1G6P complex; active site coordination in the $βPGM_{D10N}$:βG16BP complexes; comparison of backbone amide chemical shifts in the $βPGM_{D10N}$ complexes; model of the potentially catalytically competent form of the $βPGM_{D10N}$:βP1G6P complex; tables of X-ray data collection and refinement statistics, and pairwise domain rotations between the βPGM complexes (PDF).

**Accession Codes**

The atomic coordinates and structure factors have been deposited in the Protein Data Bank (www.rcsb.org) with the following codes: $βPGM_{D10N}$:$BeF_3$ complex (PDB 5OJZ),

βPGM$_{D10N}$:P1G6P complex (PDB 5OK1), co-purified βPGM$_{D10N}$:P1G6P complex (PDB 5O6P), βPGM$_{D10N}$:P6G1P complex (PDB 5OK0), βPGM$_{D10N}$:$AlF_4$:G6P complex (PDB 5OK2) and βPGM$_{D10N}$:$AlF_4$:$H_2O$:βG1P complex (PDB 5O6R). The NMR chemical shifts have been deposited in the BioMagResBank (www.bmrb.wisc.edu) with the following accession numbers: $Mg^{II}$-bound βPGM$_{D10N}$:P1G6P complex (BMRB 27174) and $Mg^{II}$-free βPGM$_{D10N}$:P1G6P complex (BMRB 27175).

AUTHOR INFORMATION

**Corresponding Author**

* E-mail for J.P.W.: j.waltho@sheffield.ac.uk

**ORCID**

Jonathan Waltho: 0000-0002-7402-5492

**Present Addresses**

¥ (L.A.J. and Y.J.) School of Chemistry, Cardiff University, Cardiff, CF10 3AT, United Kingdom

§ (C.B.) Institute of Structural and Molecular Biology, Department of Biological Sciences, Birkbeck, University of London, London, WC1E 7HX, United Kingdom

**Author Contributions**

# (L.A.J. and A.J.R.) These authors contributed equally.

**Notes**

The authors declare no competing financial interest.

ACKNOWLEDGMENTS

We would like to thank Dr Tooba Alizadeh for the preparation of the $\beta PGM_{D10N}$ plasmid construct and for the acquisition and interpretation of preliminary NMR experiments. We would also like to thank the beamline scientists at the Diamond Light Source (DLS) and the European Synchrotron Radiation Facility (ESRF) for the provision of synchrotron radiation facilities and assistance with data collection. This research was supported by the Biotechnology and Biological Sciences Research Council (N.J.B. − grant number: BB/M021637/1; C.T. − grant number: BB/K016245/1) and the Engineering and Physical Sciences Research Council (NMR spectrometer core capability − grant number: EP/K039547/1).

REFERENCES

(1) Hunter, T. Why Nature Chose Phosphate to Modify Proteins. *Phil. Trans. R. Soc. B* **2012**, *367*, 2513−2516.

(2) Lad, C.; Williams, N. H.; Wolfenden, R. The Rate of Hydrolysis of Phosphomonoester Dianions and the Exceptional Catalytic Proficiencies of Protein and Inositol Phosphatases. *Proc. Natl. Acad. Sci. U. S. A.* **2003**, *100*, 5607−5610.

(3) Buechler, J. A.; Taylor, S. S. Identification of Aspartate-184 as an Essential Residue in the Catalytic Subunit of cAMP-Dependent Protein Kinase. *Biochemistry* **1988**, *27*, 7356−7361.

(4) Green, P. C.; Tripathi, R. L.; Kemp, R. G. Identification of Active Site Residues in Pyrophosphate-Dependent Phosphofructo-1-Kinase by Site-Directed Mutagenesis. *J. Biol. Chem.* **1993**, *268*, 5085−5088.

(5) Denu, J. M.; Lohse, D. L.; Vijayalakshmi, J.; Saper, M. A.; Dixon, J. E. Visualization of Intermediate and Transition-State Structures in Protein-Tyrosine Phosphatase Catalysis. *Proc. Natl. Acad. Sci. U. S. A.* **1996**, *93*, 2493−2498.

(6) Wu, L.; Zhang, Z.-Y. Probing the Function of Asp128 in the Lower Molecular Weight Protein-Tyrosine Phosphatase-Catalyzed Reaction. A Pre-Steady-State and Steady-State Kinetic Investigation. *Biochemistry* **1996**, *35*, 5426−5434.

(7) Skamnaki, V. T.; Owen, D. J.; Nobel, M. E. M.; Lowe, E. D.; Lowe, G.; Oikonomakos, N. G.; Johnson, L. N. Catalytic Mechanism of Phosphorylase Kinase Probed by Mutational Studies. *Biochemistry* **1999**, *38*, 14718−14730.

(8) Dai, J.; Finci, L.; Zhang, C.; Lahiri, S.; Zhang, G.; Peisach, E.; Allen, K. N.; Dunaway-Mariano, D. Analysis of the Structural Determinants Underlying Discrimination Between Substrate and Solvent in β-Phosphoglucomutase Catalysis. *Biochemistry* **2009**, *48*, 1984−1995.

(9) Valiev, M.; Kawai, R.; Adams, J. A.; Weare, J. H. The Role of the Putative Catalytic Base in the Phosphoryl Transfer Reaction in a Protein Kinase: First-Principles Calculations. *J. Am. Chem. Soc.* **2003**, *125*, 9926−9927.

(10) Asthagiri, D.; Liu, T.; Noodleman, L.; Van Etten, R. L.; Bashford, D. On the Role of the Conserved Aspartate in the Hydrolysis of the Phosphocysteine Intermediate of the Low Molecular Weight Tyrosine Phosphatase. *J. Am. Chem. Soc.* **2004**, *126*, 12677−12684.

(11) Webster, C. E. High-Energy Intermediate or Stable Transition State Analogue: Theoretical Perspective of the Active Site and Mechanism of β-Phosphoglucomutase. *J. Am. Chem. Soc.* **2004**, *126*, 6840−6841.

(12) Marcos, E.; Field, M. J.; Crehuet, R. Pentacoordinated Phosphorus Revisited by High-Level QM/MM Calculations. *Proteins* **2010**, *78*, 2405−2411.

(13) Elsässer, B.; Dohmeier-Fischer, S.; Fels, G. Theoretical Investigation of the Enzymatic Phosphoryl Transfer of β-Phosphoglucomutase: Revisiting Both Steps of the Catalytic Cycle. *J. Mol. Model.* **2012**, *18*, 3169−3179.

(14) Kim, K.; Cole, P. A. Measurement of a Brønsted Nucleophile Coefficient and Insights into the Transition State for a Protein Tyrosine Kinase. *J. Am. Chem. Soc.* **1997**, *119*, 11096−11097.

(15) Zhou, J.; Adams, J. A. Is There a Catalytic Base in the Active Site of cAMP-Dependent Protein Kinase? *Biochemistry* **1997**, *36*, 2977−2984.

(16) Kim, K.; Cole, P. A. Kinetic Analysis of a Protein Tyrosine Kinase Reaction Transition State in the Forward and Reverse Directions. *J. Am. Chem. Soc.* **1998**, *120*, 6851−6858.

(17) Zhang, G.; Dai, J.; Wang, L.; Dunaway-Mariano, D.; Tremblay, L. W.; Allen, K. N. Catalytic Cycling in β-Phosphoglucomutase: A Kinetic and Structural Analysis. *Biochemistry* **2005**, *44*, 9404−9416.

(18) Dai, J.; Wang, L.; Allen, K. N.; Radstrom, P.; Dunaway-Mariano, D. Conformational Cycling in β-Phosphoglucomutase Catalysis: Reorientation of the β-D-Glucose 1,6-(Bis)phosphate Intermediate. *Biochemistry* **2006**, *45*, 7818−7824.

(19) Jin, Y.; Bhattasali, D.; Pellegrini, E.; Forget, S. M.; Baxter, N. J.; Cliff, M. J.; Bowler, M. W.; Jakeman, D. L.; Blackburn, G. M.; Waltho, J. P. α-Fluorophosphonates Reveal How a Phosphomutase Conserves Transition State Conformation Over Hexose Recognition in Its Two-Step Reaction. *Proc. Natl. Acad. Sci. U. S. A.* **2014**, *111*, 12384−12389.

(20) Baxter, N. J.; Bowler, M. W.; Alizadeh, T.; Cliff, M. J.; Hounslow, A. M.; Wu, B.; Berkowitz, D. B.; Williams, N. H.; Blackburn, G. M.; Waltho, J. P. Atomic Details of Near-Transition State Conformers for Enzyme Phosphoryl Transfer Revealed by $MgF_3^-$ Rather Than by Phosphoranes. *Proc. Natl. Acad. Sci. U. S. A.* **2010**, *107*, 4555−4560.

(21) Baxter, N. J.; Olguin, L. F.; Goličnik, M.; Feng, G.; Hounslow, A. M.; Bermel, W.; Blackburn, G. M.; Hollfelder, F.; Waltho, J. P.; Williams, N. H. A Trojan Horse Transition State Analogue Generated by $MgF_3^-$ Formation in an Enzyme Active Site. *Proc. Natl. Acad. Sci. U. S. A.* **2006**, *103*, 14732−14737.

(22) Baxter, N. J.; Hounslow, A. M.; Bowler, M. W.; Williams, N. H.; Blackburn, G. M.; Waltho, J. P. $MgF_3^-$ and α-Galactose 1-Phosphate in the Active Site of β-Phosphoglucomutase Form a Transition State Analogue of Phosphoryl Transfer. *J. Am. Chem. Soc.* **2009**, *131*, 16334−16335.

(23) Griffin, J. L.; Bowler, M. W.; Baxter, N. J.; Leigh, K. N.; Dannatt, H. R. W.; Hounslow, A. M.; Blackburn, G. M.; Webster, C. E.; Cliff, M. J.; Waltho, J. P. Near Attack Conformers

Dominate β-Phosphoglucomutase Complexes Where Geometry and Charge Distribution Reflect Those of Substrate. *Proc. Natl. Acad. Sci. U. S. A.* **2012**, *109*, 6910−6915.

(24) Jin, Y.; Richards, N. G. J.; Waltho, J. P.; Blackburn, G. M. Metal Fluorides as Analogues for Studies on Phosphoryl Transfer Enzymes. *Angew. Chem. Int. Ed.* **2017**, *56*, 4110−4128.

(25) Jin, Y.; Molt, R. W.; Blackburn, G. M. Metal Fluorides: Tools for Structural and Computational Analysis of Phosphoryl Transfer Enzymes. *Top. Curr. Chem.* **2017**, *375*, 36−59.

(26) Bruice, T. C. Some Pertinent Aspects of Mechanism as Determined With Small Molecules. *Annu. Rev. Biochem.* **1976**, *45*, 331−374.

(27) Jin, Y.; Molt, R. W.; Waltho, J. P.; Richards, N. G. J.; Blackburn, G. M. $^{19}$F NMR and DFT Analysis Reveal Structural and Electronic Transition State Features for RhoA-Catalyzed GTP Hydrolysis. *Angew. Chem. Int. Ed.* **2016**, *55*, 3318−3322.

(28) Jin, Y.; Molt, R. W.; Pellegrini, E.; Cliff, M. J.; Bowler, M. W.; Richards, N. G. J.; Blackburn, G. M.; Waltho, J. P. Assessing the Influence of Mutation on GTPase Transition States Using X-Ray Crystallography, $^{19}$F NMR and DFT Approaches. *Angew. Chem. Int. Ed.* **2017**, *56*, 9732−9735.

(29) Reed, M. A. C.; Hounslow, A. M.; Sze, K. H.; Barsukov, I. G.; Hosszu, L. L. P.; Clarke, A. R.; Craven, C. J.; Waltho, J. P. Effects of Domain Dissection on the Folding and Stability of the 43 kDa Protein PGK Probed by NMR. *J. Mol. Biol.* **2003**, *330*, 1189−1201.

(30) Goličnik, M.; Olguin, L. F.; Feng, G.; Baxter, N. J.; Waltho, J. P.; Williams, N. H.; Hollfelder, F. Kinetic Analysis of β-Phosphoglucomutase and Its Inhibition by Magnesium Fluoride. *J. Am. Chem. Soc.* **2009**, *131*, 1575−1588.

(31) Vranken, W. F.; Boucher, W.; Stevens, T. J.; Fogh, R. H.; Pajon, A.; Llinas, M.; Ulrich, E. L.; Markley, J. L.; Ionides, J.; Laue, E. D. The CCPN Data Model for NMR Spectroscopy: Development of a Software Pipeline. *Proteins* **2005**, *59*, 687−696.

(32) Schulte-Herbrüggen, T.; Sørensen, O. W. Clean TROSY: Compensation for Relaxation-Induced Artefacts. *J. Magn. Reson.* **2000**, *144*, 123−128.

(33) Lescop, E.; Schanda, P.; Brutscher, B. A Set of BEST Triple-Resonance Experiments for Time-Optimized Protein Resonance Assignment. *J. Magn. Reson.* **2007**, *187*, 163−169.

(34) Hyberts, S. G.; Robson, S. A.; Wagner, G. Exploring Signal-to-Noise Ratio and Sensitivity in Non-Uniformly Sampled Multi-Dimensional NMR Spectra. *J. Biomol. NMR* **2013**, *55*, 167−178.

(35) Hyberts, S. G.; Milbradt, A. G.; Wagner, A. B.; Arthanari, H.; Wagner, G. Application of Iterative Soft Thresholding for Fast Reconstruction of NMR Data Non-Uniformly Sampled With Multidimensional Poisson Gap Scheduling. *J. Biomol. NMR* **2012**, *52*, 315−327.

(36) Sun, Z.-Y. J.; Frueh, D. P.; Selenko, P.; Hoch, J. C.; Wagner, G. Fast Assignment of $^{15}$N-HSQC Peaks Using High-Resolution 3D HNcocaNH Experiments With Non-Uniform Sampling. *J. Biomol. NMR* **2005**, *33*, 43−50.

(37) Williamson, M. P. Using Chemical Shift Perturbation to Characterise Ligand Binding. *Prog. Nucl. Magn. Reson. Spectrosc.* **2013**, *73*, 1−16.

(38) Pellegrini, E.; Piano, D.; Bowler, M. W. Direct Cryocooling of Naked Crystals: Are Cryoprotection Agents Always Necessary? *Acta Cryst.* **2011**, *D67*, 902−906.

(39) Winter, G. *xia2:* An Expert System for Macromolecular Crystallography Data Reduction. *J. Appl. Cryst.* **2010**, *43*, 186−190.

(40) Battye, T. G. G.; Kontogiannis, L.; Johnson, O.; Powell, H. R.; Leslie, A. G. W. iMOSFLM: A New Graphical Interface for Diffraction-Image Processing With MOSFLM. *Acta Cryst.* **2011**, *D67*, 271−281.

(41) Vagin, A.; Teplyakov, A. MOLREP: An Automated Program for Molecular Replacement. *J. Appl. Cryst.* **1997**, *30*, 1022−1025.

(42) Emsley, P.; Lohkamp, B.; Scott, W. G.; Cowtan, K. Features and Development of COOT. *Acta Cryst.* **2010**, *D66*, 486−501.

(43) Murshudov, G. N.; Vagin, A. A.; Dodson, E. J. Refinement of Macromolecular Structures by the Maximum-Likelihood Method. *Acta Cryst.* **1997**, *D53*, 240−255.

(44) Chen, V. B.; Arendall, W. B.; Headd, J. J.; Keedy, D. A.; Immormino, R. M.; Kapral, G. J.; Murray, L. W.; Richardson, J. S.; Richardson, D. C. MolProbity: All-Atom Structure Validation for Macromolecular Crystallography. *Acta Cryst.* **2010**, *D66*, 12−21.

(45) The PyMOL Molecular Graphics System, Version 1.8. (Schrödinger, LLC, 2015).

(46) Read, R. J.; Schierbeek, A. J. A Phased Translation Function. *J. Appl. Cryst.* **1988**, *21*, 490−495.

(47) Hayward, S.; Berendsen, H. J. C. Systematic Analysis of Domain Motions in Proteins From Conformational Change: New Results on Citrate Synthase and T4 Lysozyme. *Proteins* **1998**, *30*, 144−154.

(48) Lahiri, S. D.; Zhang, G.; Radstrom, P.; Dunaway-Mariano, D.; Allen, K. N. Crystallization and Preliminary X-Ray Diffraction Studies of β-Phosphoglucomutase From *Lactococcus lactis*. *Acta Cryst.* **2002**, *D58*, 324−326.

(49) Lahiri, S. D.; Zhang, G.; Dunaway-Mariano, D.; Allen, K. N. Caught in the Act: The Structure of Phosphorylated β-Phosphoglucomutase From *Lactococcus lactis*. *Biochemistry* **2002**, *41*, 8351−8359.

(50) Lahiri, S. D.; Zhang, G.; Dunaway-Mariano, D.; Allen, K. N. The Pentacovalent Phosphorus Intermediate of a Phosphoryl Transfer Reaction. *Science* **2003**, *299*, 2067−2071.

(51) Tyler-Cross, R.; Schirch, V. Effects of Amino Acid Sequence, Buffers, and Ionic Strength on the Rate and Mechanism of Deamidation of Asparagine Residues in Small Peptides. *J. Biol. Chem.* **1991**, *266*, 22549−22556.

(52) Rowland, R. S.; Taylor, R. Intermolecular Nonbonded Contact Distances in Organic Crystal Structures: Comparison With Distances Expected From van der Waals Radii. *J. Phys. Chem.* **1996**, *100*, 7384−7391.

(53) Baxter, N. J.; Blackburn, G. M.; Marston, J. P.; Hounslow, A. M.; Cliff, M. J.; Bermel, W.; Williams, N. H.; Hollfelder, F.; Wemmer, D. E.; Waltho, J. P. Anionic Charge Is Prioritized Over Geometry in Aluminum and Magnesium Fluoride Transition State Analogs of Phosphoryl Transfer Enzymes. *J. Am. Chem. Soc.* **2008**, *130*, 3952−3958.

(54) Woolley, E. M.; Tomkins, J.; Hepler, L. G. Ionization Constants for Very Weak Organic Acids in Aqueous Solution and Apparent Ionization Constants for Water in Aqueous Organic Mixtures. *J. Solution Chem.* **1972**, *1*, 341−351.

(55) Shen, Y.; Bax, A. Protein Backbone and Sidechain Torsion Angles Predicted From NMR Chemical Shifts Using Artificial Neural Networks. *J. Biomol. NMR* **2013**, *56*, 227−241.

(56) Barrozo, A.; Liao, Q.; Esguerra, M.; Marloie, G.; Florian, J.; Williams, N. H.; Kamerlin, S. C. L. Computer Simulations of the Catalytic Mechanism of Wild-Type and Mutant β-Phosphoglucomutase. *Org. Biomol. Chem.* **2018**, *16*, 2060−2073.

(57) Zamberlin, Š.; Antunac, N.; Havranek, J.; Samaržija, D. Mineral Elements in Milk and Dairy Products. *Mljekarstvo* **2012**, *62*, 111−125.

(58) Kerns, S. J.; Agafonov, R. V.; Cho, Y.-J.; Pontiggia, F.; Otten, R.; Pachov, D. V.; Kutter, S.; Phung, L. A.; Murphy, P. N.; Thai, V.; Alber, T.; Hagan, M. F.; Kern, D. The Energy Landscape of Adenylate Kinase During Catalysis. *Nat. Struct. Mol. Biol.* **2015**, *22*, 124−131.

TOC GRAPHIC

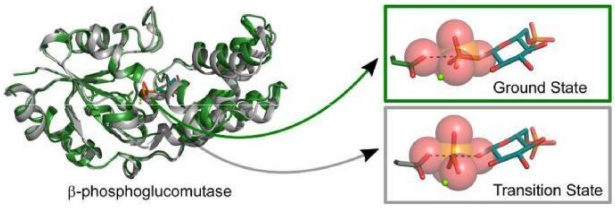

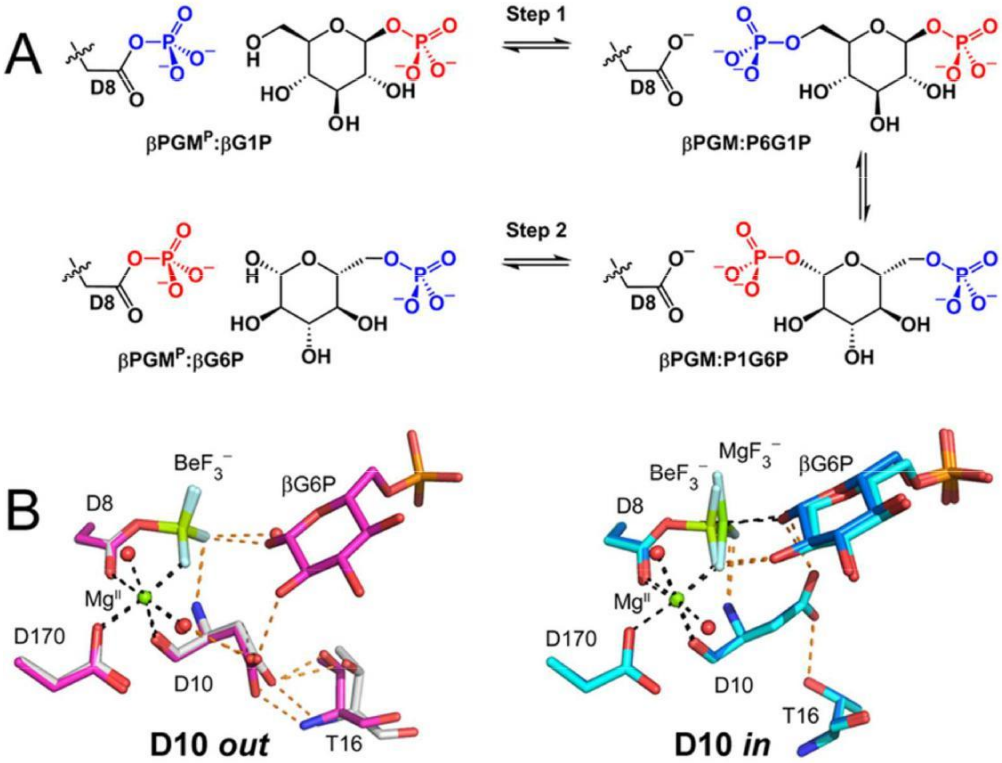


68x53мм (300 x 300 DPI)

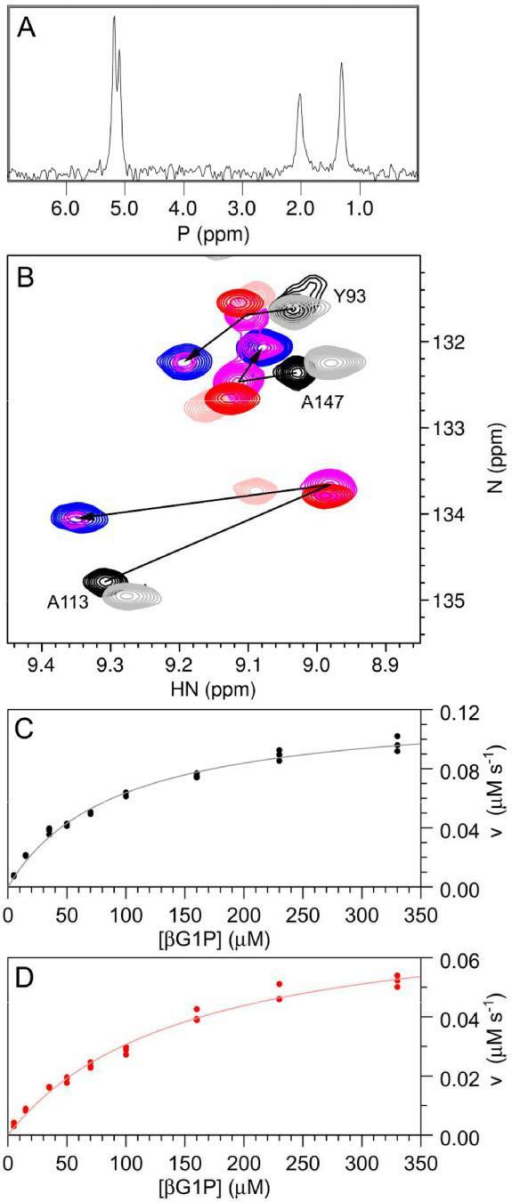


204x480мм (300 x 300 DPI)

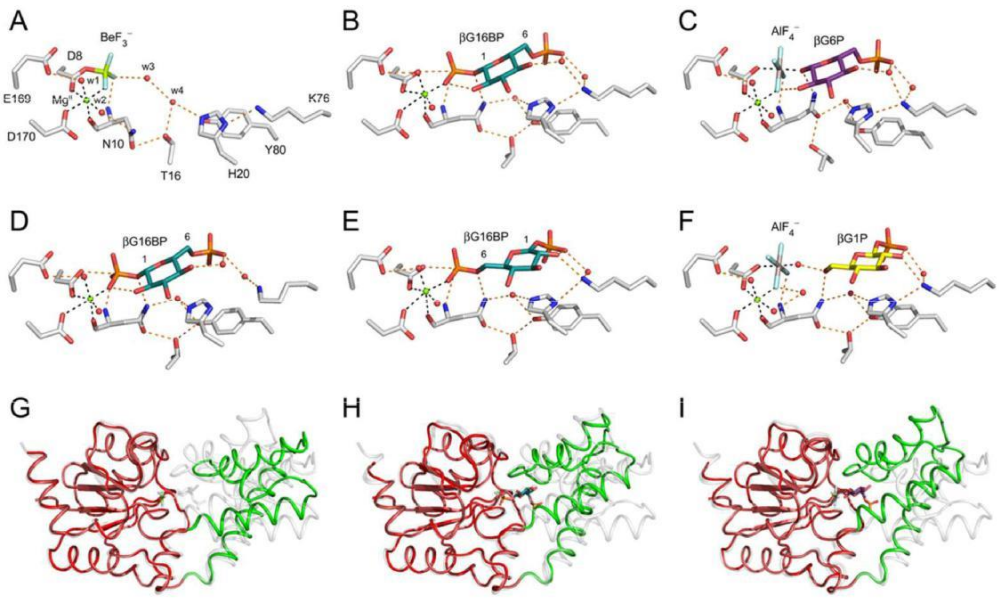


105x63mm (300 x 300 DPI)

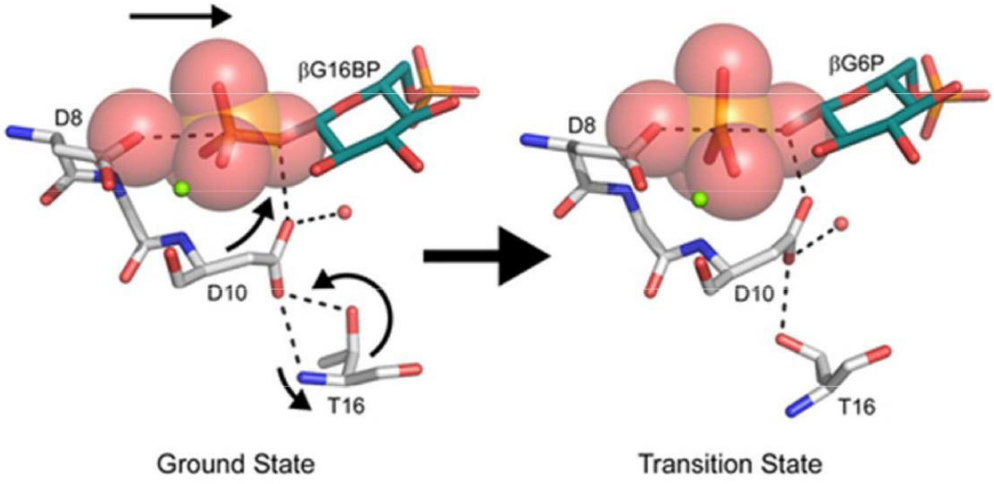


42x20mm (300 x 300 DPI)

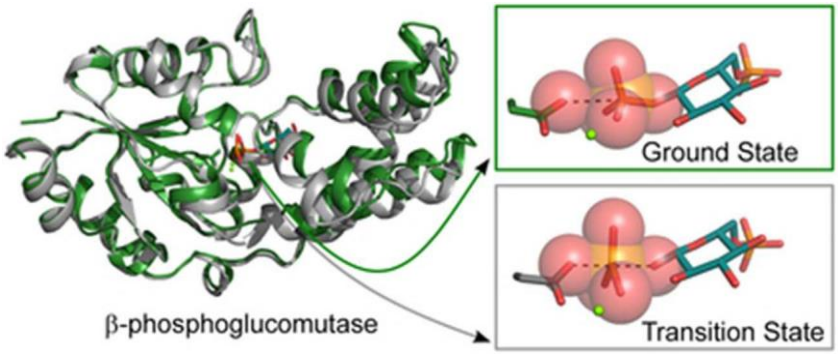


35x14mm (300 x 300 DPI)